Earthquakes Source Scaling at Subfault Scales

Margarita M. Solares-Colón[1†] and Diego Melgar[1]

[1]Department of Earth Sciences, University of Oregon, Eugene, Oregon, U.S.A.

Corresponding author: Margarita M. Solares-Colón (msolares@uoregon.edu)

†Present address: School of Earth Sciences, The Ohio State University, Columbus, Ohio, USA.

Author ORCIDs

Margarita M. Solares-Colón: 0000-0002-9387-7551

Diego Melgar: 0000-0001-6259-1852

Author contributions

Conceptualization: M. M. Solares-Colón, D. Melgar

Formal Analysis: M. M. Solares-Colón, D. Melgar

Investigation: M. M. Solares-Colón

Methodology: M. M. Solares-Colón, D. Melgar

Funding Acquisition: D. Melgar

Project Administration: D. Melgar

Supervision: D. Melgar

Visualization: M. M. Solares-Colón, D. Melgar

Writing – original draft: M. M. Solares-Colón

Writing – review & editing: M. M. Solares-Colón, D. Melgar

Key Points:

- Systematic analysis of moderate-to-large earthquakes using finite-fault models to evaluate source properties.
- In general, shorter rise times are observed, consistent with pulse-like rather than crack-like rupture behavior.
- At the subfault scale, local rise time shows no correlation with slip, challenging a common assumption in earthquake modeling.

Abstract

Establishing scaling laws for large earthquakes remains challenging due to the heterogeneity of methodologies and datasets used to produce finite-fault models. In this study, we analyze source properties for 264 earthquakes using the NEIC finite-fault database, expanding previous efforts by examining rupture behavior over a broader magnitude range and capturing both established scaling trends and variability at the subfault scale. In general, pulse-like ruptures are favored over propagating crack-like ruptures with shorter rise times. At the subfault scale, the common assumption of rise time ($\tau \propto \sqrt{s}$) is not sustained by the observations and slip rate strongly correlates with slip. These findings are significant because pulse-like ruptures, characterized by shorter rise times and higher slip rates, have important implications for the resulting ground motions, potentially affecting regions farther from the source depending on where slip is concentrated. These local variations are important for earthquake modeling and can improve downstream applications such as rupture simulations, thereby advancing our understanding of earthquake processes.

Plain Language Summary

Understanding how earthquakes start and grow helps scientists estimate their potential impacts, but this remains difficult because earthquake models are created using different methods and data types. To better understand these differences, we combine and analyze information from a large global database of earthquake models developed by the U.S. Geological Survey's National Earthquake Information Center (NEIC). By comparing hundreds of earthquakes of different sizes and fault types, we look for consistent patterns in how faults move in space and evolve through time. Findings from this study will improve our understanding of earthquake behavior and help refine models used to assess earthquake hazards and simulate future events.

1 Introduction

Characterizing kinematic source parameters—such as slip, rupture dimensions, rupture velocity, and rise time—in relation to earthquake size remains a fundamental pursuit in seismology (Somerville et al., 1999; Mai & Beroza, 2000; Ye et al., 2016; Melgar & Hayes, 2017). These efforts are aimed at understanding earthquake physics and assessing the predictability of rupture behavior. Scaling laws provide a framework that links earthquake observations to the

underlying rupture dynamics that govern how rupture propagation evolves with earthquake size. A common assumption is self-similarity (Aki, 1967), which holds that earthquake sources are scale-invariant, meaning that the physical processes remain similar across magnitudes and scale by a constant factor. With the growing number of well-recorded earthquakes—from teleseismic (Ye et al., 2016; Melgar & Hayes, 2017) to strong motion (Mai & Thingbaijam, 2014) and geodetic observations (Shea & Barnhart, 2022), kinematic models of large earthquakes are often derived using heterogeneous datasets and methodologies. This variability in earthquake modeling is inevitable because of incremental advances in instrumentation, computing power, and analytical techniques, combined with data availability constraints on near-source observations imposed by tectonic setting (e.g., offshore trenches) or restrictions on data access due to local policies. As a result, establishing consistent scaling laws for earthquakes is increasingly challenging, which makes the synthesis of general behaviors ambiguous.

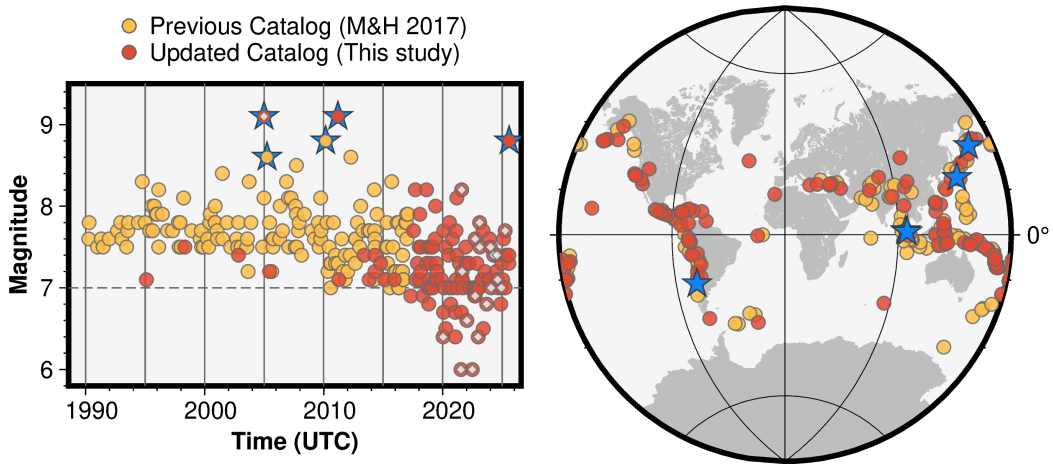

Figure 1. Magnitude time series and map view of the NEIC Finite-Fault model database. Events from the Melgar & Hayes (2017) catalog (yellow circles) and the expanded catalog presented in this study (red-orange circles) are shown here. After the NEIC finite-fault code was upgraded to include regional data (i.e., strong motion, GNSS and InSAR observation), events with mixed datasets (light colored diamonds) are highlighted in the magnitude time series. Vertical gray lines indicate regular temporal intervals of every 5 years. Blue Stars show the top five largest events recorded in the database (**M**9.1 Sumatra 2004, **M**9.1 Tohoku 2011, **M**8.8 Maule 2010, **M**8.8 Kamchatka 2025, and **M**8.6 Nias 2005 earthquakes).

Finite-fault models provide a means of extracting information about earthquake source properties. In this study, we analyze the global archive of finite-fault models produced by the U.S. Geological Survey-National Earthquake Information Center (USGS-NEIC; Hayes, 2017), building on Melgar & Hayes (2017). We extend their work by incorporating 115 additional events, including those that occurred after their study, as well as events more recently processed by the USGS-NEIC (e.g., the **M**9.1 2004 Sumatra earthquake) or revisited as part of this analysis (e.g.,

the **M**9.1 2011 Tohoku earthquake). This expanded dataset enables us to refine general trends observed across the seismic spectrum in previous work (**Figure 1**) and to further examine rupture behavior at the subfault scale, adding detail beyond event-averaged finite-fault properties. We are particularly interested in the scaling of source parameters for moderate-to-large earthquakes, which are difficult to characterize because of the complexity and nonlinearity of rupture processes. In attempts to simplify or linearize the problem, it is often necessary to assume certain parameters to be constant, such as rise time or rupture velocity. Our goal is to evaluate source parameters such as slip, rise time, and slip rate that we can solve for using a nonlinear inversion method, and to test whether the data are consistent with self-similarity at general (i.e., mean values) scale and what occurs at the local (i.e., subfaults) scale.

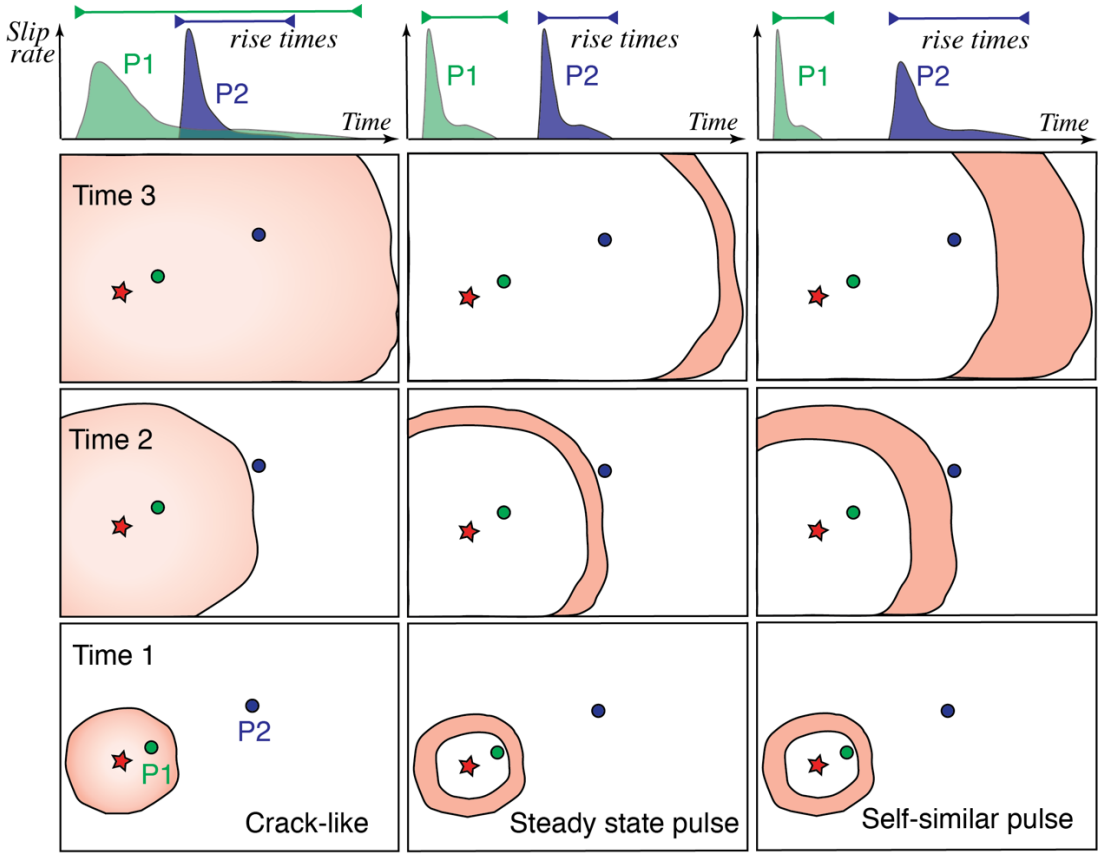

Figure 2. Earthquake rupture styles. Each column illustrates an end-member rupture behavior, ranging from crack-like to pulse-like: (1) crack-like, (2) steady-state pulse, and (3) self-similar pulse. The top row shows the slip-rate function and the corresponding time evolution of slip, with two reference time points (P1 and P2) indicated. The remaining three rows present snapshots of rupture propagation through time, from Time 1 (bottom) to Time 3 (top). In the crack-like case (first column), the rupture front expands continuously and terminates only when the earthquake ends. In contrast, the pulse-like ruptures (second and third columns) exhibit both a propagating front and a healing front: the steady-state pulse maintains a constant width, whereas the self-similar pulse grows in size as the rupture evolves.

The limitations of resolving kinematic parameters such as rise time in finite-fault inversions have been explored from both methodological and physical perspectives. For instance, Konca et al. (2013) assessed how accurately kinematic inversions using seismic and geodetic data could recover slip, rise time, and rupture velocity from dynamic rupture simulations. Their results revealed strong trade-offs among these, showing that rise time is difficult to resolve due to regularization effects, highlighting the non-uniqueness of kinematic solutions. Expanding on this, Somala et al. (2014) quantified the physical limits imposed by network geometry and rupture kinematics, demonstrating that for sub-Rayleigh ruptures, rise times shorter than about 2 s can only be resolved with station spacing of roughly ≤ 5 km, whereas supershear ruptures are better resolved at coarser spacing (up to few tens of kilometers) because the energy decay is much slower. To address these limitations and evaluate the consistency of the recovered source parameters from finite-fault models produced by the USGS-NEIC, we compare inversion results for a subset of events from three independent studies as a validation step.

Distinguishing these parameters is important for assessing the suitability of different conceptual models of the earthquake rupture process. Seismologists often distinguish between two main rupture styles: crack-like (Kostrov, 1964) and pulse-like (Brune, 1970; Heaton, 1990). These models describe how slip evolves on the fault as rupture progresses (**Figure 2**). In a crack-like rupture, a single rupture front propagates along the fault until the earthquake terminates. The slip duration at a given point, the rise time, extends from the arrival of the rupture front until rupture arrest, lasting close to the total source duration. In contrast, a pulse-like rupture behaves as a “self-healing” slip pulse. The fault slips briefly as the rupture front passes, followed by a healing front that halts slip so that its duration at a point is only a fraction of the total source duration. Dynamic rupture simulations further demonstrate that pulse-like ruptures can occur in different forms (Gabriel et al., 2012). Decaying pulses weaken with distance, growing pulses strengthen as they propagate, and steady-state pulses maintain nearly constant properties. Which type develops depends primarily on the background stress and the size of the nucleation region.

Why does the distinction matter? Because it shapes both rupture dynamics and the characteristics of ground shaking (Heaton, 1990; Ben-Zion, 2001; Wang & Day, 2017). A crack-

like rupture releases energy gradually over an extended interval, whereas a pulse-like rupture concentrates the energy release into short bursts. These differences influence the amount, timing, and frequency content of the seismic energy radiated from the fault. Crack-like ruptures, by sustaining slip for most of the source duration, are associated with longer-period signals and generally lower ground motions. Pulse-like ruptures, in contrast, release energy in short bursts that radiate high frequencies, producing stronger ground motions, particularly in the near-source region.

2 Finite Fault database and modeling

Finite-fault models were obtained from the USGS–NEIC database, which includes events from 1990 to 2025, concluding with the **M**8.8 Kamchatka earthquake on 29 July 2025 (**Figure 1**). These models are routinely produced, with human oversight for general quality assurance and control. For large events, there can be several updates, sometimes weeks or months after the event, as new information and observations become available. The catalog of Melgar & Hayes (2017) is here expanded by ~77% (from 149 to 264 events), broadening the magnitude range to span **M**6 - **M**9. The augmented catalog incorporates 20 events with regional data (strong motion, GNSS and InSAR observations), thereby improving coverage at moderate magnitudes (**M**6s).

The legacy NEIC inversion code for finite-fault modeling initially relied solely on teleseismic data for earthquakes of **M** ≥ 7 (Hayes, 2017). In 2021, it was updated to integrate regional datasets—including static and high-rate GNSS, InSAR, and strong-motion, where available—by implementing Wavelet and simulated Annealing SliP (WASP; Koch et al., 2024) software as described in Goldberg et al. (2022). WASP (now Wavelet Inversion for SliP (WISP); Goldberg et al., 2026) employs a nonlinear inversion approach based on Ji et al. (2002), as used in the legacy version, and the framework from Koch et al. (2019), to jointly invert teleseismic and regional observations. On a discretized fault plane, the inversion estimates slip amplitude, rake (slip direction), rise time, and rupture onset time for each subfault. The time history of slip is described by an asymmetric cosine source time function, which represents the slip-rate evolution. As a result of these innovations, the USGS–NEIC dataset now includes joint inversions of several significant recent and past events, such as the 2004 **M**9.1 Sumatra earthquake, which combined teleseismic data and GNSS static offsets to model the longest fault rupture on record

(~570 s). For this study, we reprocessed the 2011 **M**9.1 Tohoku earthquake using teleseismic data only to investigate constraints in rise time values (more details in following section) and included the 2020 **M**6.4 southwestern Puerto Rico mainshock (Solares-Colón et al., 2025) inverted with WISP using teleseismic and regional data, filling a gap in the mid-**M**6 magnitude range.

3 Non-linear inversion method validation

3.1 Comparison of WISP inversion and other independent inversion methods

In this work we present results of earthquake source scaling properties at the subfault scale. An important question is whether these source properties retrieved by WISP are reliable and consistent with what is imaged using other independent approaches. To assess this, we selected three finite-fault models developed with independent methodologies for comparison. It is important to note that the vast majority of slip models in the literature are obtained through linearized inversion approaches, which do not reliably retrieve key kinematic parameters such as rise time. We therefore focus on models derived from fully non-linear approaches. Two of the selected finite-fault models follow Bayesian methods described in Minson et al. (2014) applied to the 2011 **M**9.1 Tohoku (Minson et al., 2014) and the 2014 **M**8.2 Iquique (Duputel et al., 2015) earthquakes. The third model implements the Bayesian Earthquake Analysis Tool (BEAT; Vasyura-Bathke et al., 2020), as applied to the 2021 **M**7.4 Maduo earthquake (Suhendi et al., 2025). In contrast to WISP's asymmetric cosine source-time function, the Minson et al. (2014) inversions adopt a triangular slip-velocity function, while the BEAT inversion used here assumes a half-cosine source-time function (Lay et al., 2010). These differences could potentially lead to distinct representations of slip-rate evolution across the three methods to evaluate.

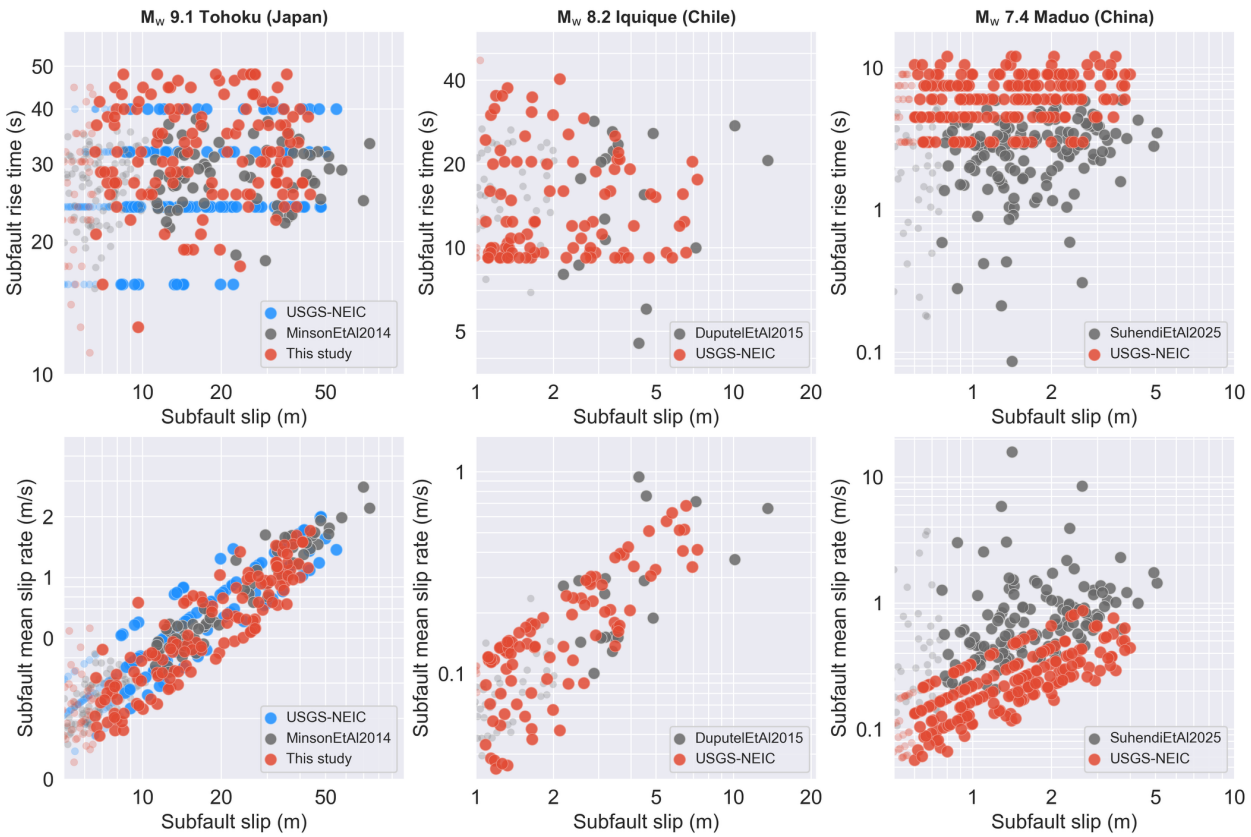

Figure 3. Comparison across independent rupture models for three earthquakes: **M**9.1 Tohoku 2011, **M**8.2 Iquique 2014, and **M**7.4 Maduo 2021. Each column corresponds to one event; the top row shows subfault slip versus rise time, and the bottom row shows subfault slip versus mean slip rate for the same datasets. Gray markers denote published models (Tohoku: Minson et al., 2014; Iquique: Duputel et al., 2015; Maduo: Suhendi et al., 2025), and red–orange markers show the USGS–NEIC products. For Tohoku, we also include a re-run of the NEIC inversion to assess striking artifacts related to restrictive rise-time bounds. Subfaults with slip ≥ 15% of the event peak slip are emphasized; lower-slip patches are shown smaller and with increased transparency for context.

Figure 3 shows the comparison of the NEIC finite-fault models from the catalog used in this study with corresponding models derived from alternative approaches for subfaults with ≥ 15% of the event maximum slip. While some variations are evident, the important result is that general trends remain consistent, with similar patterns observed for rise time (no correlation with slip) and slip rate (high correlation with slip). For the great Tohoku earthquake, one of only two **M**9 events in the catalog, the currently available USGS-NEIC model shows an evident streaking effect (blue circles in first column of **Figure 3**) due to the inversion being parametrized in a way that allowed only a very limited set of rise-time values when it was carried out. To address this, we re-inverted this event with WISP, allowing for a broader range of rise-time values and using teleseismic data only, to be consistent with the original release (orange-red circles in first column of **Figure 3**). For the Maduo earthquake, discrepancies between the NEIC teleseismic-only solution and regionally constrained models are more apparent (third column of

199 **Figure 3**). However, if we further restrict the comparison to subfaults with rise time ≥ 1 s—below
200 which teleseismic and InSAR data offer limited constraints due to their low-frequency sensitivity
201 (as discussed in the introduction) and static nature (Funning et al., 2013), respectively—the rise
202 time and slip rate patterns show closer agreement with those observed in the other two events.
203 As noted by Funning et al. (2013), InSAR alone cannot constrain temporal of parameters of a
204 rupture, though geodetic observations complement seismic observations in joint inversions as
205 also demonstrated in Goldberg et al. (2022). Still, such short rise time values remain difficult to
206 resolve without near-field strong-motion and sufficient station density (Somala et al., 2014).
207 We emphasize that the NEIC models used here are teleseismic-only, whereas the
208 comparison models more extensively examine and incorporate regional strong-motion, GNSS,
209 InSAR, and even tsunami data in the case of Tohoku. Despite these differences in data coverage
210 and uncertainties in fault plane geometry, the NEIC models still yields source parameter ranges
211 consistent with independent models. Such consistency, we contend, validates WISP results and
212 supports the use of the catalog for first-order analyses of earthquake source scaling relations.

213 3.2 Comparison of WISP teleseismic-only and joint inversions

214 As the NEIC now routinely produces slip models using combined datasets, the finite-fault
215 model database continues to grow within a unified inversion framework. Goldberg et al. (2022)
216 demonstrated the reliability of joint inversions by comparing teleseismic-only and joint solutions
217 for the same earthquakes in a rapid response context. We use the four earthquakes analyzed in
218 Goldberg et al. (2022) to evaluate whether the WISP framework systematically biases source
219 parameter values or expands their observed ranges when joint data are included. These events
220 include the 2015 **M**8.3 Illapel (Chile), the 2021 **M**8.2 Chignik (Alaska), the 2021 **M**7.3 Nippes
221 (Haiti), and the 2020 **M**6.0 Antelope Valley (California).

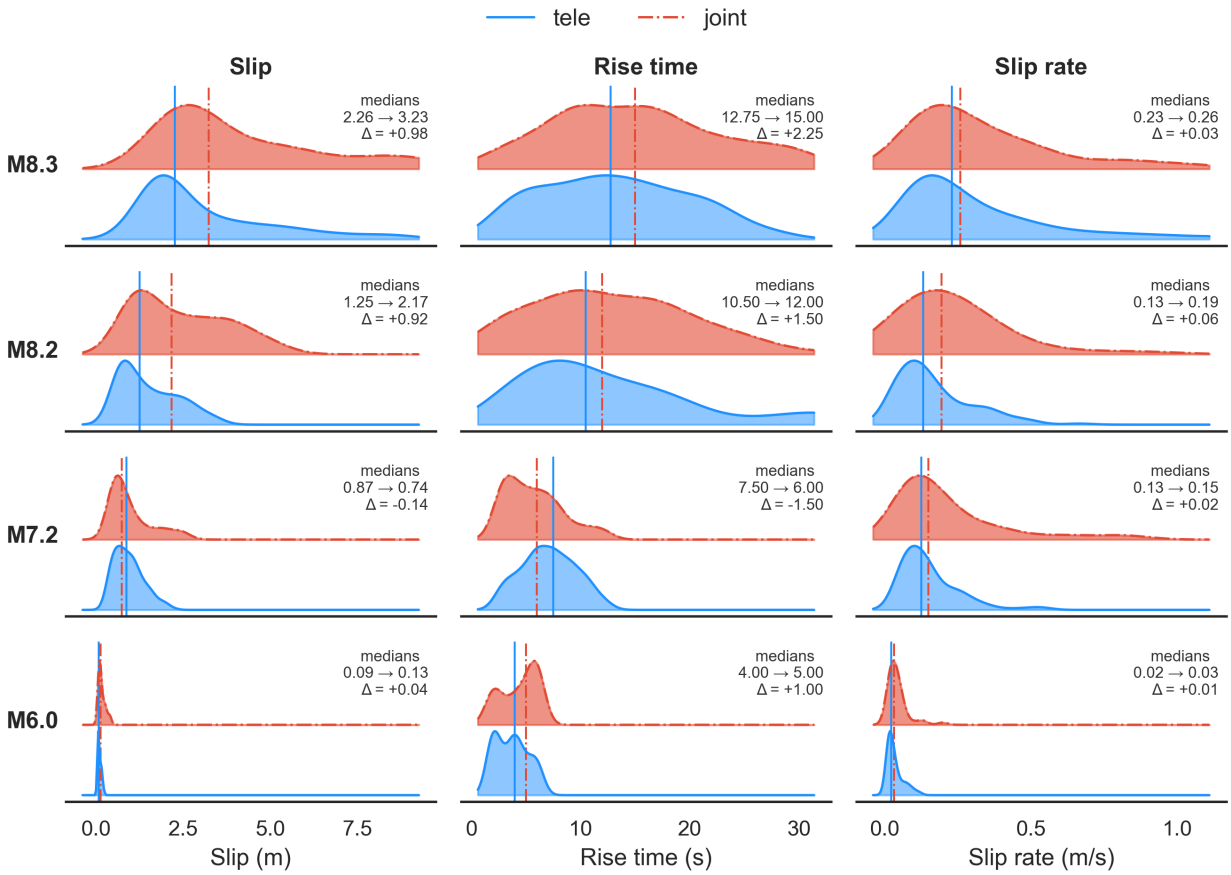

Figure 4. Comparison of WISP rupture models using teleseismic data only versus joint inversions with mixed datasets for four earthquakes from Goldberg et al. (2022): **M**8.3 Illapel (Chile) 2015, **M**8.2 Chignik (Alaska, USA) 2021, **M**7.3 Nippes (Haiti) 2021and **M**6.0 Antelope Valley (California, USA) 2021. Each row corresponds to one event, and each column shows subfault source parameters (slip, rise time, and slip rate). Blue color corresponds to teleseismic-only NEIC inversion models, while red-orange color corresponds to joint inversion models for the same earthquakes. Vertical lines mark the median of each rupture model and source parameter pair. The median value per inversion correspond to the numerical values shown in the upper-right legend for teleseismic-only and joint inversions; Δ indicates the change between these two inversion approaches.

Source parameters were examined as a function of slip using the same plotting format as in **Figure 3**; however, the comparison here focuses on teleseismic-only versus joint WISP solutions rather than independent versus WISP inversions. We observe comparable ranges of rise time and slip rate for both inversion solutions across events (refer to **Figure S2** in Supplementary Information). To better characterize their distributional behavior, we then examined the corresponding probability density functions shown as ridge plots in **Figure 4**. Both teleseismic-only and joint solutions show right-skewed distributions. Despite these similarities in shape per event-parameter pair, important deviations emerge upon closer inspection. Rise time exhibits the largest median shift ($|\Delta| \geq 1$) of the three parameters analyzed. Joint inversions display wider spread and increased density towards the higher values relative to teleseismic-only inversions,

particularly for larger events (**M** > 8), indicating greater source variability resolved by the combined data types. At smaller magnitude (**M** < 8) of these four events, discrepancies between WISP solutions are more pronounced. Slip and slip rate distributions exhibit a wider spread in joint inversions, whereas rise time distribution in both tele and joint inversions develop secondary peaks or local maxima, resulting in distinct morphologies. While these irregular shapes may represent true rupture complexity, they could also be partially attributed to data noise or inversion artifacts. Especially for smaller events, lower signal-to-noise ratios make distinguishing physical complexity from numerical noise more challenging than for larger earthquakes. Despite these limitations, the inclusion of regional data provides a unique advantage: by being closer to the source and accessing broader frequency bandwidths, joint inversions can capture finer-scale characteristics that are otherwise lost to attenuation in teleseismic-only models.

4 Results & Discussion

4.1 General behaviors: Event-Averaged Source Scaling and Self-Similarity

In this analysis, we examine kinematic source properties derived from finite-fault models and revisit the self-similar assumption, which posits that earthquake source properties scale with event size and can be expressed as power-law functions of seismic moment:

$$\log_{10}(S) = a + b\log_{10}(M_0), \qquad (1)$$

where S is the source parameter of interest, M_0 is seismic moment, a is a constant, and b is the scaling exponent. The scaling exponent b is estimated as the slope of a linear fit in log–log space, based on the fault-averaged source parameter values for each parent earthquake. Self-similarity is assessed by comparing the fitted slope with the expected value ($b \approx 1/3$ for slip and rise time; $b \approx 0$ for slip rate). To further constrain these relationships, we estimate posterior distributions of the regression parameters using a Bayesian approach (refer to **Text S1** in Supplementary Material for more details), allowing us to refine existing scaling laws and extend the results from Melgar & Hayes (2017) (refer to **Table S1** and **Figure S1** for scaling laws in Supplementary Material).

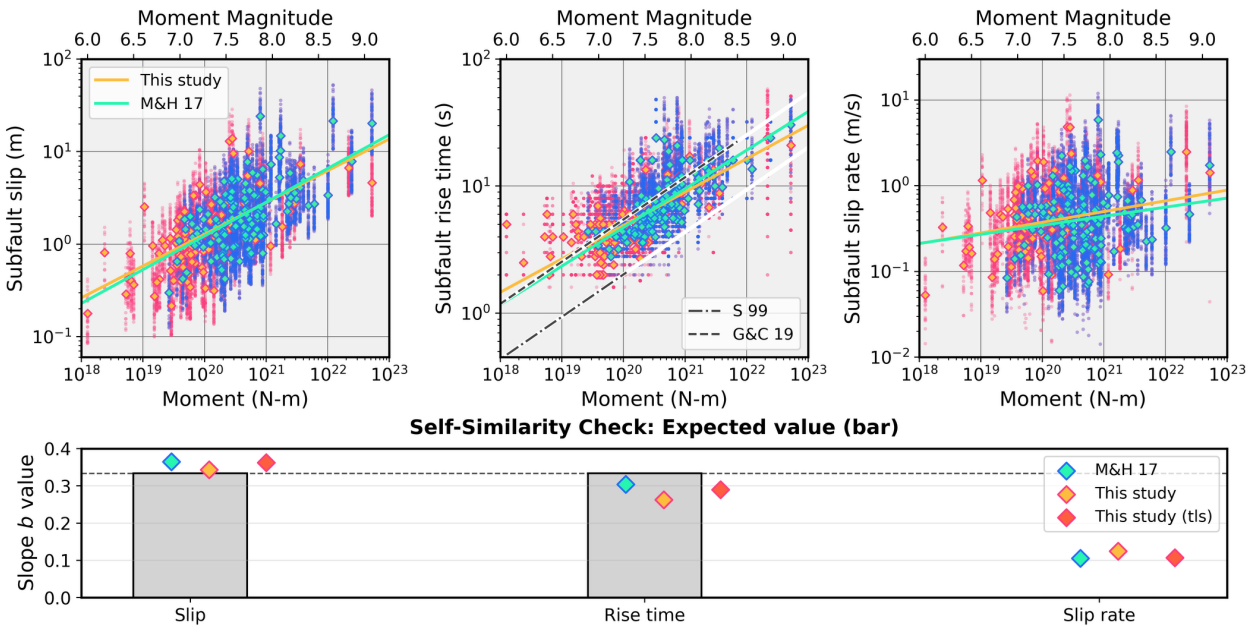

Figure 5. Testing Self-similarity of earthquake source parameters. Top row: log–log scatter plots of subfault slip (left), rise time (middle), and slip rate (right) versus seismic moment of the NEIC finite-fault database. Melgar & Hayes (2017) catalog is shown in cool colors (blues, cyan), while newly added events in this study are shown in warm colors (dark pink and yellow). Circles represent subfaults with >20% of the maximum slip of each parent earthquake, lines show fitted linear trends through all subfaults, and diamonds indicate mean values. Rise-time scaling from Somerville et al. (1999) refer to as S 99 (dark gray dotted-dashed line) and from Gusev & Chebrov (2019) refer to as G&C 19 (dark gray dashed line); white lines show extrapolated trends toward larger magnitudes. Bottom row: slope value (scaling exponent) estimates of the log–log regressions for each source parameter. Bars indicate the expected self-similar value (1/3 for slip and rise time; 0 for slip rate), and scatter markers show the b-value for each catalog. This summary plot highlights how scaling behavior may deviate from self-similar expectations across different magnitude ranges and between catalogs.

Source parameters are plotted as a function of seismic moment for all subfaults within each parent earthquake (colored circles in **Figure 5**). Note that we used subfaults with ≥ 20% of the event slip maximum to minimize the influence of inversion artifacts and retained only nonzero values for rise time, onset time, and hypocenter distance. To highlight updated catalog from Melgar & Hayes (2017), hereafter referred to as M&H17, events added in this study are plotted in warm colors, while those that appear in both catalogs are shown in cool colors. Now, for the average over the entire fault area of a given earthquake (colored diamonds in **Figure 5**), rise time scales more weakly than the cube root of seismic moment (b = 0.263), indicating a more sublinear trend towards pulse-like behavior, and slip scaling remains self-similar (b = 0.343). Consequently, slip rate scaling flattens, and no longer scales with earthquake size in a meaningful way as in M&H17 (refer to **Figure S3** in Supplementary Information). Such scaling behavior is consistent with its dependence on both slip (s) and rise time (τ) under self-similarity assumptions, where slip rate is defined as $\dot{s} = s/\tau$. This relation assumes constant stress drop and rupture

290 geometry: as seismic moment increases, fault length grows, and both slip and rise time increase
291 in proportion to that length (Somerville et al., 1999). As a result, the observed slight increase in
292 slip rate indicates that rise time grows more slowly (i.e., shorter τ) relative to slip, as the
293 proportionality between slip and rise time is no longer preserved. This observation does not
294 necessarily imply slower rupture propagation but rather a more pulse-like character on average,
295 in which larger earthquakes release slip more rapidly at each point, even though the total rupture
296 duration could last longer.

297 Compared with the scaling of average rise time proposed by Somerville et al. (1999)
298 (hereafter refer to as S99; dark gray dotted-dashed line in the middle panel of the top row in
299 **Figure 5**) several nuances are worth noting. S99 used rupture models of crustal earthquakes
300 primarily inferred from low-pass filtered strong motion data, the proximity of these near-fault
301 recordings provides finer temporal resolution than the teleseismic waveforms that represents
302 longer-period behavior dominated by large subduction events in the NEIC database. Their models
303 thus yield and can capture smaller rise times than those inferred from teleseismic inversions. The
304 differences in data bandwidth, magnitude range, and tectonic setting partly explain why trends
305 do not overlap as discussed by M&H17, and by extension observed here. However, Gusev &
306 Chebrov (2019) (dark gray dashed-line in the middle panel of the top row in **Figure 5**) later
307 reanalyzed strong-motion derived finite-fault models from the SRCMOD catalog (Mai &
308 Thingbaijam, 2014) and compared their results with both earlier studies (S99 and M&H17). By
309 using a consistent measure of average rise time (T_r) across source elements (i.e., subfaults) and
310 expanding the magnitude range, they found that rise time estimates from modern strong-motion
311 rupture models converge toward the longer rise times consistent with teleseismic analyses. This
312 reconciliation implies that the offset between datasets likely reflects methodological choices
313 instead of inherent physical differences, as noted by Gusev & Chebrov (2019), in how rise time is
314 defined for asymmetric slip pulses. They observed that earlier inversions often inferred rise time
315 based on the time to peak slip rate, providing a truncated measure of source duration and
316 consequently yielding shorter rise time values. By comparison, newer analyses resolve the full
317 slip-history evolution, from onset to arrest, producing longer rise time estimates that capture the
318 temporal complexity of slip across the fault. In this context, the evolution from S99 to Gusev &

Chebrov (2019) represents a methodological shift, finding consistency of the $T_r \propto M_0^{1/3}$ scaling across data types. Therefore, the catalogs are complementary rather than directly comparable, highlighting different portions of the earthquake spectrum, from near-field behavior to global rupture characteristics.

Overall, pulse-like ruptures remain favored over crack-like ruptures, with rise times generally shorter than the total source duration. This is consistent with the findings from M&H17 that also explored whether the WISP inversion framework tended to bias results toward pulse-like ruptures. As in this study, their normalized rise-time distributions were skewed toward the lower end of the allowed range (refer to **Figure S4** in Supplementary Information). They further examined high-rate GNSS data and found that stations near large events consistently showed static offset growth durations shorter than the total source duration (refer to **Figure 3** in Melgar & Hayes, 2017), reinforcing the interpretation of predominantly pulse-like rupture behavior. However, departures from self-similar scaling do emerge, trending toward smaller scaling exponent b. This trend is more pronounced when teleseismic and regional datasets are combined. The impact of incorporating regional data on inferred source-parameter scaling remains to be determined. Retrospective analyses of finite fault models, including regional observations where available, will provide a more complete picture.

4.2 Subfault Scale Behavior: Source Scaling with Slip

Variations at the subfault scale are important when modeling earthquakes. A common assumption, especially for kinematic and semi-stochastic modeling, is that the local rise time (τ_r) is proportional to the square root of slip (s) scaled by a constant (k), and expressed as

$$\tau_r = k\sqrt{s}. \qquad (2)$$

In this formulation, larger slip patches are expected to exhibit longer rise times. This slip–rise time correlation was first introduced by Aagaard et al. (2008) as a physically based assumption calibrated against observations of the 1989 Loma Prieta earthquake to simulate ground motions. It was later adopted by Graves & Pitarka (2010) in stochastic and kinematic simulations to reproduce those physical constraints in synthetic ruptures and subsequently implemented in

finite-fault modeling frameworks (e.g., Melgar et al., 2016) and has been used in other reduced-physics modeling frameworks. Here, we examine whether this empirical relationship holds across the NEIC finite-fault catalog and how it manifests across magnitudes and subfault scale.

Figure 6 shows rise time and slip rate as a function of slip for all subfaults in the database. If we focused on the subfaults of the largest events (**M** ≥ 8.8; green stars in scatterplots of **Figure 6**): (1) rise times shows no evident dependence on slip and (2) slip rates increase linearly with slip. The patterns observed here are consistent with those in **Figure 3**: rise time shows no clear correlation with slip, whereas slip rate correlates strongly with slip. Although the rise time scatter plot offers limited clarity, the expected slip–rise time correlation ($\tau_r \propto \sqrt{s}$) is notably absent.

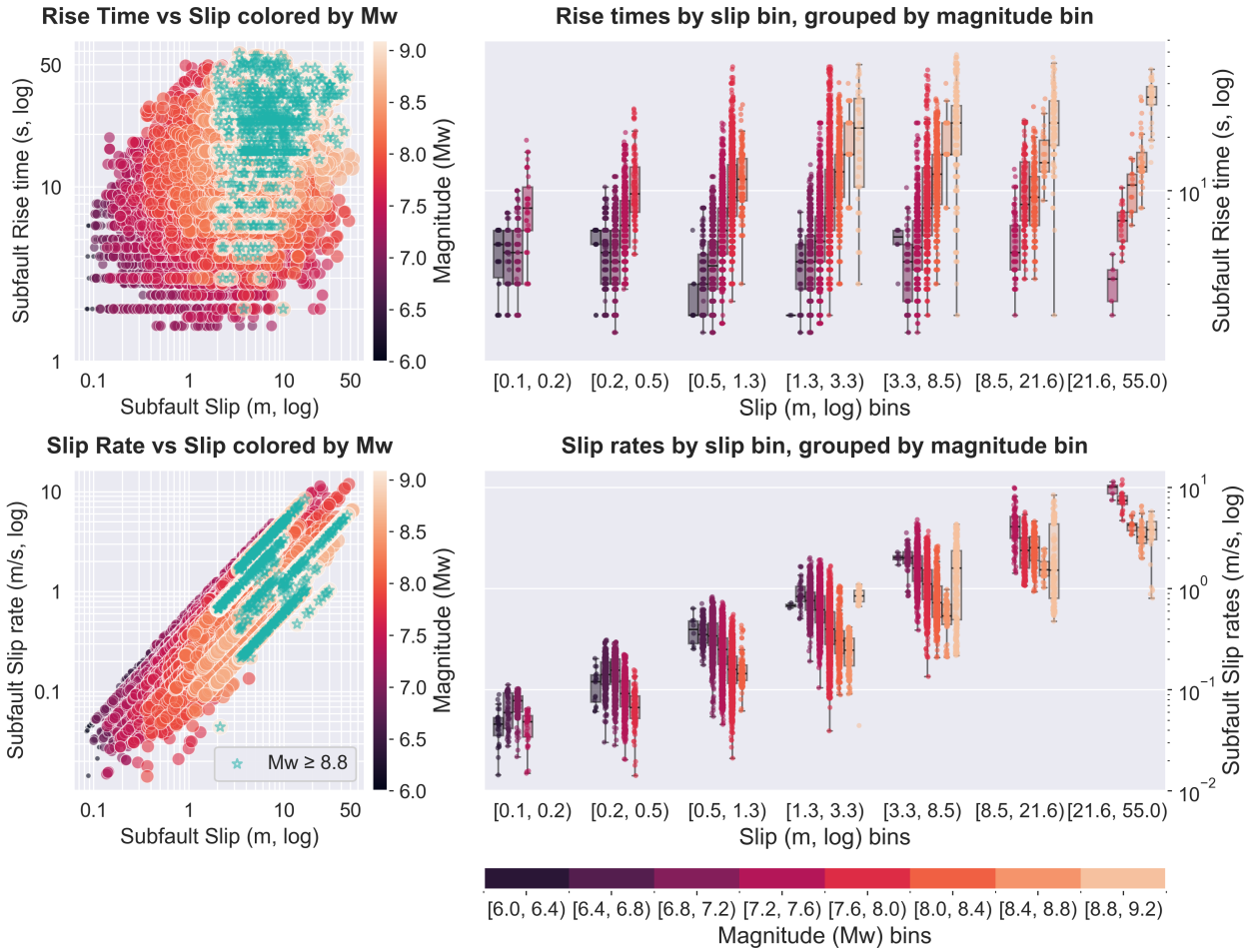

Figure 6. Local behaviors of source parameters at the subfault scale. The first panel shows rise time (top) and slip rate (bottom) as functions of slip, with markers colored by magnitude; green stars represent subfaults of the largest events (M ≥ 8.8). The second panel presents boxplots of the same parameters, where subfaults are first binned by slip, and within each bin values are grouped by magnitude—corresponding to the scatter plots in the first panel.

To further examine these relationships, we mapped scatterplot data to boxplots, illustrating how rise time and slip rate vary with slip across magnitudes (**Figure 6**). Rise time distributions vary slightly with slip when comparing to same magnitude bin across slip bins, but within each slip bin, rise time grows with magnitude. This shows that self-similarity holds internally, with longer rise times and larger slip values continuing to scale with magnitude, yet it differs from the expected slip–rise time correlation that rise time scales with local slip. In contrast, slip rate distributions increase with slip when comparing to same magnitude bin across slip bins. More interestingly, slip rates show the opposite trend to rise times within slip bins, tending to decrease with magnitude, except for very large to great earthquakes (**M** ≥ 8.8) that increases abruptly indicating a potential shift in scaling behavior. At the subfault scale, observations indicate that larger slips are accommodated by higher slip rate (i.e., the fault sliding faster), rather than through longer slip durations (i.e., wider pulses). These findings depart from those of dynamic rupture simulations, which show correlation between slip and rise time, as reported by Schmedes et al. (2010). More recent results from Petukhin et al. (2025), however, indicate that rise time exhibits weaker correlation with slip, whereas slip rate remains more strongly correlated with other rupture parameters, consistent with the observations in this study.

4.2.1 Source Properties by Fault Type

We also subdivided the dataset by fault type to assess potential biases and local processes in source parameters of interest as a function of slip for all subfaults in the database (refer to **Figures S5** and **S6** for rise time and slip rate distributions, respectively, in Supporting Information). While WISP includes fault parameters derived from moment tensor solutions and a velocity model, it lacks explicit geological or topographic constraints. Even so, the results indicate that thrust events are characterized by higher slip and longer rise times than other fault types in the database. This is particularly true for subduction megathrust earthquakes, which have also been shown to exhibit depth dependence (Lay et al., 2012; Kurahashi & Irikura, 2011; Kiser & Ishii, 2012; Melgar et al., 2016; Cárdenas et al., 2023). The elongation of rise times is most pronounced in the shallow portion of the megathrust, where rupture tends to propagate more slowly and radiate less high-frequency energy than at greater depths. In contrast, strike-slip events generally display shorter rise times than thrust events and higher slip rates than other

389 fault type in the database. The simpler geometry of large crustal strike-slip faults allows
390 supershear rupture propagation (Bouchon et al., 2010), in which the rupture front moves faster
391 than the shear-wave velocity and radiates high-frequency energy over greater distances from the
392 source (Andrews, 2010), resulting in shorter rise times and faster slip. Lastly, normal events,
393 smallest subset of the database (48 events), exhibit lower rise times and slip rates relative to
394 other fault types. Quantitative studies of source properties for normal-faulting events are scarcer
395 than for strike-slip events, which are generally easier to parameterize, and for megathrust events,
396 which have received greater attention due to their earthquake size and hazard potential.
397 Although several well-documented normal and normal-oblique events—such as the 2009 **M**6.1
398 L'Aquila in Italy (not in this study nor NEIC database; Cirella et al., 2012) and the 2020 **M**6.4
399 Southwestern Puerto Rico Seismic Sequence mainshock (included in this study database; Solares-
400 Colón et al., 2025) events, demonstrate that moderate earthquakes can produce complex
401 rupture processes, though broader generalizations remain limited.

402 4.2.2 A First Direct Benchmark for Source Properties

403 Considering noise and artifacts inherent in finite-fault inversions, some subfaults exhibit
404 very high slip velocity (over 10 m/s) across fault types. Dynamic and experimental studies indicate
405 typical upper bounds on slip rate of ~6–10 m/s for crustal, sub-shear events, with higher values
406 possible under supershear or extreme stress conditions (Andrews, 2005; Schmedes et al., 2010;
407 Bizzarri, 2012; Gabriel et al., 2013). This peak slip rate limit emerges from the dynamic coupling
408 between rupture velocity and growth of slip velocity, governed by the final slip, stress drop, and
409 the fracture energy required to sustain propagation. A recent real-world example of a supershear
410 crustal strike-slip earthquake is the 2025 **M**7.8 Myanmar event on the Sagaing Fault. The rupture
411 extended for more than 450 km, with average slip of ~3–6 m, a source duration exceeding 80 s,
412 and reaching rupture speeds of 4–6 km/s (Diao et al., 2025; Melgar et al., 2025; Vera et al., 2025;
413 Wei et al., 2025; Xu et al., 2025; Ye et al., 2025). Closed-circuit television (CCTV) footage from a
414 camera located ~20 m east of the Sagaing Fault and ~120 km south of the hypocenter captured
415 surface rupture and allowed direct estimation of earthquake source properties (Kearse & Kaneko,
416 2025; Latour et al., 2025). Independent analyses of CCTV footage yielded consistent near-field
417 estimates of fault slip during this event. Both studies found slip amplitudes of ~2.5–3 m, durations

of ~1.3–1.4 s, and peak slip velocities of ~3.2–3.5 m/s, providing direct constraints on rupture kinematics. These findings represent a first benchmark for rupture evolution analyses and serve as ground truth for rupture model validation of large crustal earthquakes. They also reveal pulse-like characteristics in large earthquakes, consistent with the general sublinear trend toward pulse-like behavior observed in the NEIC finite-fault database (**Figure 5**). The onset or transition to supershear propagation in rupture models varies among studies; however, Latour et al. (2025) inferred that the portion of the rupture observed by the CCTV camera propagated at a locally sub-shear velocity. Based on this interpretation, we could infer that supershear propagation may produce higher peak slip rates than those observed at sub-shear velocity, approaching the upper bound of 6–10 m/s range proposed by dynamic rupture models.

4.3 Testing Slip–Rise Time Correlation

If local rise time scales with slip, then the expectation is that larger slip patches will exhibit longer rise times and wider pulses. However, the present dataset does not support this assumption at the subfault scale. Rise time shows no dependence on local slip remaining roughly constant across slip bins (**Figure 6** for subfault behavior of source parameters), which indicates that slip pulses are relatively steady, but increase with earthquake size (refer to **Figure S3** for mean subfault pulse-length scaling with moment), conserving self-similarity (refer to **Figure 5** for general mean behavior of source parameters).

To assess whether pulses grow or remain constant as rupture evolves, we examine rise time as a function of distance from the hypocenter and onset time for each subfault (first two columns of **Figure 7**). Scatter plots for distance and onset time in **Figure 7** do not show a clear linear trend and instead form a diffuse point cloud with an apparent positive relationship. This pattern most likely arises from combining events of different magnitudes and is controlled by overall event size and duration, rather than reflecting pulse growth during rupture propagation (refer to first row of **Figure 7**, where highlighted subfaults correspond to events with **M** ≥ 8.8). However, when considering onset time, the cloud of points becomes more scattered at earlier stages of rupture propagation. To better capture the duration of slip at each subfault, we examine the end time versus onset time (third column of **Figure 7**). This representation provides a proxy

for potentially distinguishing crack-like from pulse-like rupture behavior (refer to **Figure 2** for earthquake rupture styles). The vertical distance from the one-to-one line represents the rise time, $\tau_r = t_{\text{end}} - t_{\text{onset}}$; therefore, points farther from the line correspond to subfaults with longer slip durations. Notably, the dataset indicates a transition in rupture behavior (Gabriel et al., 2012), in which rupture may initiate in a more crack-like manner and evolve toward pulse-like behavior as it propagates (Meier et al., 2016). To account for potential biases, we also colored data points by slip and depth (second and third row of **Figure 7**). For slip, no clear pattern is observed, and the variability likely reflects heterogeneity associated with asperities, rupture dimensions, and rupture directivity. For depth, observations are consistent with previous findings that shallow regions of the rupture exhibit longer rise times than deeper regions.

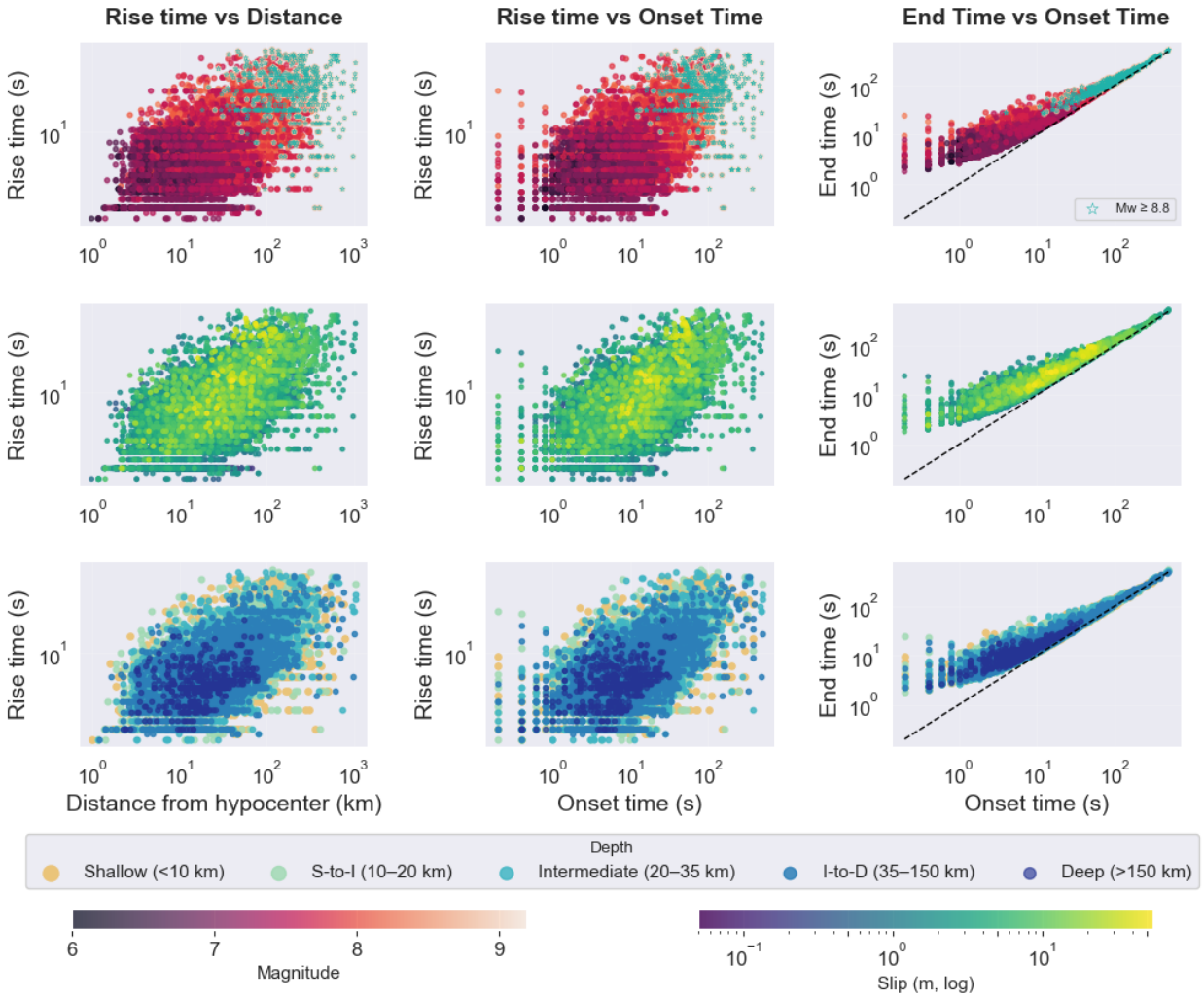

Figure 7. Local rise time against distance and onset time for each subfault per parent earthquake. The first column shows rise time as a function of distance from the hypocenter. Markers in the first row are colored by magnitude, and green stars represent subfaults

459 of the largest events (M ≥ 8.8). Markers in the second row are colored by slip, and markers in the third row are colored by depth.
460 The second column shows rise times versus onset time with the same marker coloring. The third column shows end-time versus
461 onset time; the vertical distance from the one-to-one line represents the rise time, $\tau_r = t_{\text{end}} - t_{\text{onset}}$.

462 Whether these are steady or growing pulses cannot be robustly resolved without event-
463 by-event analysis or normalization across magnitudes and rupture durations. This reflects the
464 challenge of comparing subfault scale behavior across events that span a wide range of sizes,
465 rupture durations, and fault types, particularly in a dataset largely constrained by teleseismic
466 observations. Therefore, we explore rupture behavior through simulations with different slip–
467 rise time assumptions to probe pulse evolution during rupture propagation.

468 To test the impact of the slip–rise time assumption, we ran a semi-stochastic kinematic
469 rupture model of a **M**8.78 Cascadia simulation under two rise time assumptions: case (1) with a
470 prescribed slip–rise time correlation (Eq. 2) and case (2) with no dependence of rise time on slip
471 following the methods described in Melgar et al. (2016) and using the scaling exponent from
472 M&H17, to better illustrate behaviors of source parameter (i.e., rise time and slip rate) as the
473 pulse front develops. **Figure 8** shows snapshots of the rupture evolution. For each case, slip rate
474 and slip are shown, with the first pair corresponding to case (1) and the second pair to case (2).
475 The final panel shows the difference in slip rate between the two cases. We find that for case (1),
476 pulse width increases when the rupture front passes through high-slip patches (northern part of
477 the rupture) and decreases in lower-slip regions (more visible towards the southern region of the
478 rupture). In contrast, for case (2), pulse width remains relatively constant when rupture front
479 passes through high/low-slip areas. Although the differences may appear subtle at first, the
480 clearest contrast is in the peak slip rates. Case (2) produces locally higher peak slip rates when
481 the rupture front encounters high-slip patches, reaching values that are approximately 50%
482 larger than in Case (1) for subfaults within a selected region (refer to **Figure S7** in Supplementary
483 Information). Rather than being accommodated through a pulse-widening effect (i.e., longer rise
484 times), as in case (1), these high-slip patches are expressed as sharper, localized increases in peak
485 slip rate. Generally, high-slip rates are linked to stronger ground shaking by generating high-
486 frequency bursts that alter the frequency content of the seismic energy radiated from the fault.
487 These differences are significant because pulse-like ruptures with higher slip rates and shorter
488 pulses (i.e., shorter rise times) have important implications for the resulting ground motions that

489 can affect regions farther from the source. Thus, they impact earthquake modeling and may lead
490 to underestimation of seismic hazards, depending on where slip is concentrated, and requires
491 further investigation.

492

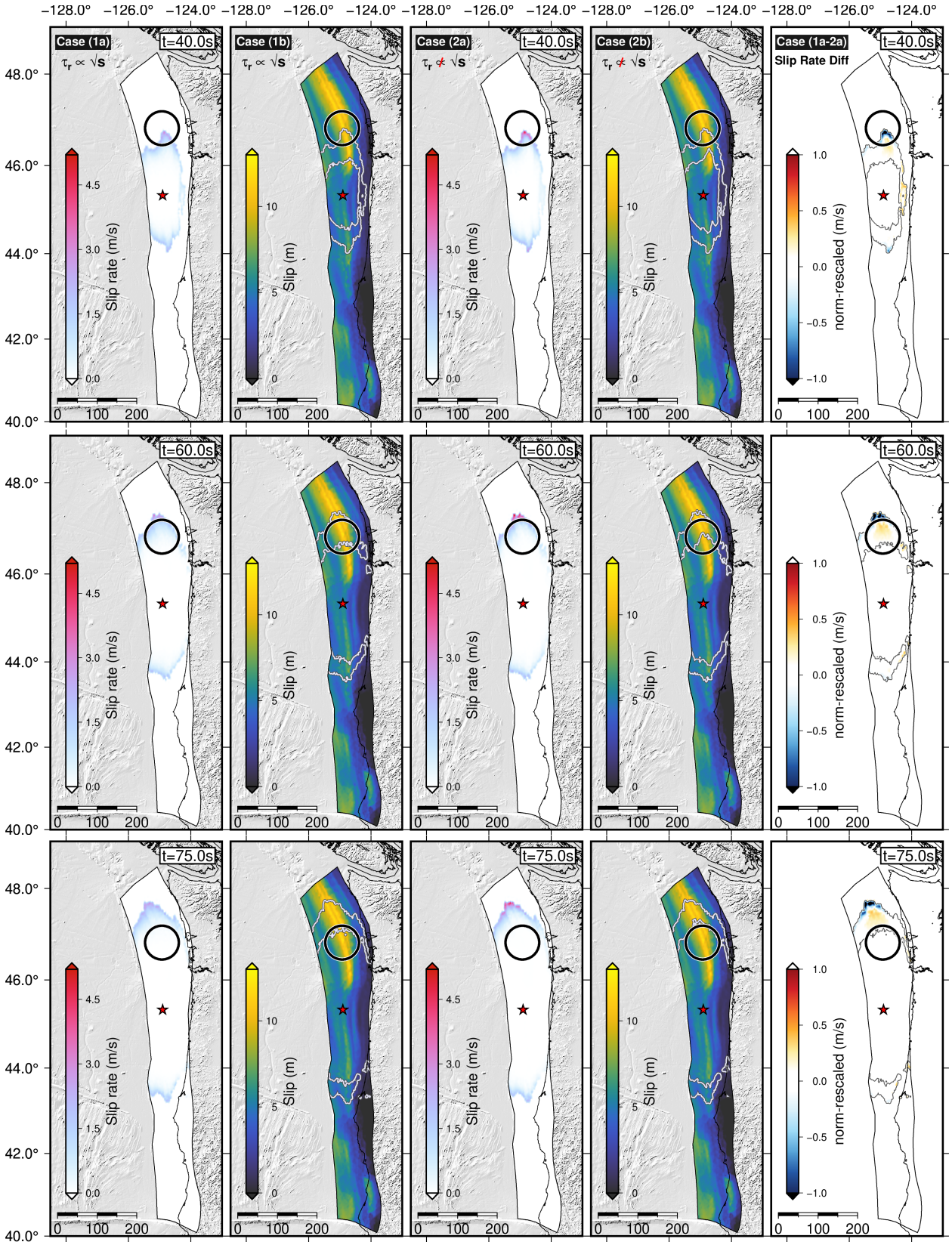

Figure 8. Snapshots of a **M**8.78 Cascadia rupture simulation under two rise-time assumptions: case (1) has a prescribed correlation between rise time and slip (Eq. 2; scaling exponent from Melgar & Hayes, 2017), whereas case (2) assumes no dependence of rise time on slip. Each of the three rows shows a different time step in the rupture evolution, with five panels per row: the first two panels show slip rate and slip for case (1); the next two panels show the same quantities for case (2); and the last panel shows the slip-rate difference between them. Blue indicates areas where case (2) produces higher slip rates, and red indicates areas where case (1) produces higher slip rates; black circles are focus points to compare slip pulse width. The full rupture sequence is provided in Video S1 of the Supplementary Information**.**

5 Implications for earthquake modeling and concluding remarks

This study analyzes a catalog of 264 finite-fault models produced by the USGS-NEIC to evaluate source properties over a wider range of magnitudes (**M** 6.0–9.1) with a systematic inversion approach. As a validation step, we also compare to other independent finite-fault models for consistency in source parameters ranges. We focus on finite-fault models inferred from non-linear approaches to estimate not only slip distributions but also other source parameters of interest, such as rise time and slip rate, which allow us to examine rupture kinematics from general behaviors down to the subfault scale. Although these models do not directly resolve local stress or energy, spatial patterns in rise time and slip rate serve as useful kinematic proxies for underlying dynamic processes. Such information becomes increasingly important for downstream applications, including earthquake simulations and predictive frameworks. In describing the general behavior of earthquakes, self-similarity remains broadly consistent, though deviations emerge, with pulse-like ruptures continuing to be favored over propagating-crack models, building on the work of Melgar & Hayes (2017). However, at the subfault scale, the common assumption of rise time proportionality to the square root of slip is not sustained by the observations.

Determining the specific contribution of each data type to the final joint solution remains a focal point of interest for seismologist. As new inversion techniques capable of jointly inverting teleseismic, geodetic, strong-motion, and tsunami data continue to advance reprocessing past well-recorded events remains essential to ensure that legacy earthquakes are represented with modern methods and extending to progressively smaller magnitudes. Retrospective analyses of slip distributions therefore remain essential for assessing the general characteristics of earthquake source parameters.

Acknowledgments

We are thankful to Dara Goldberg and Jean-Paul Ampuero for their constructive feedback and discussions in the initial phase of this study. We also recognized the work and ongoing efforts at the NEIC to provide quality products for earthquake science. ChatGPT (OpenAI) was used to assist

with language editing during the preparation of this manuscript. The authors are responsible for all scientific content.

Open Research

The NEIC finite-fault models were obtained from the ANSS Comprehensive Earthquake Catalog (https://earthquake.usgs.gov/earthquakes/search/). The finite-fault models used in this study are provided as text files in the Supplementary Data hosted on Zenodo (Solares-Colón & Melgar, 2026). The Wavelet and Simulated Annealing SliP (WASP; now WISP) inversion code used to obtain the slip models is publicly available on GitLab (Koch et al., 2024). The code used for the source properties analysis is available on GitHub and is also archived in Zenodo repository (Solares-Colón & Melgar, 2026). PyMC4 (Abril-Pla et al., 2023) was used to perform the MCMC analysis and estimate the posterior distributions of the regression parameters.

Conflict of Interest Disclosure

The authors declare there are no conflicts of interest for this manuscript.

References

Aagaard, B. T., Brocher, T. M., Dolenc, D., Dreger, D., Graves, R. W., Harmsen, S., Hartzell, S., Larsen, S., & Zoback, M. L. (2008). Ground-Motion Modeling of the 1906 San Francisco Earthquake, Part I: Validation Using the 1989 Loma Prieta Earthquake. *Bulletin of the Seismological Society of America*, *98*(2), 989–1011. https://doi.org/10.1785/0120060409

Abril-Pla, O., Andreani, V., Carroll, C., Dong, L., Fonnesbeck, C. J., Kochurov, M., Kumar, R., Lao, J., Luhmann, C. C., Martin, O. A., Osthege, M., Vieira, R., Wiecki, T., & Zinkov, R. (2023). PyMC: A modern, and comprehensive probabilistic programming framework in Python. PeerJ Computer Science, 9, e1516. https://doi.org/10.7717/peerj-cs.1516

Aki, K. (1967). Scaling law of seismic spectrum. *Journal of Geophysical Research*, *72*(4), 1217–1231. https://doi.org/10.1029/JZ072i004p01217

543 Andrews, D. J. (2005). Rupture dynamics with energy loss outside the slip zone. *Journal of Geophysical*
544 *Research: Solid Earth*, *110*(B1), 2004JB003191. https://doi.org/10.1029/2004JB003191
545 Andrews, D. J. (2010). Ground motion hazard from supershear rupture. *Tectonophysics*, *493*(3–4), 216–
546 221. https://doi.org/10.1016/j.tecto.2010.02.003
547 Ben-Zion, Y. (2001). Dynamic ruptures in recent models of earthquake faults. *Journal of the Mechanics*
548 *and Physics of Solids*, *49*(9), 2209–2244. https://doi.org/10.1016/S0022-5096(01)00036-9
549 Bizzarri, A. (2012). Rupture speed and slip velocity: What can we learn from simulated earthquakes?
550 *Earth and Planetary Science Letters*, *317–318*, 196–203. https://doi.org/10.1016/j.epsl.2011.11.023
551 Bouchon, M., Karabulut, H., Bouin, M.-P., Schmittbuhl, J., Vallée, M., Archuleta, R., Das, S., Renard, F., &
552 Marsan, D. (2010). Faulting characteristics of supershear earthquakes. *Tectonophysics*, *493*(3–4),
553 244–253. https://doi.org/10.1016/j.tecto.2010.06.011
554 Brune, J. N. (1970). Tectonic stress and the spectra of seismic shear waves from earthquakes. *Journal of*
555 *Geophysical Research*, *75*(26), 4997–5009. https://doi.org/10.1029/JB075i026p04997
556 Cárdenas, D. R., Miller, M., & Montalva, G. A. (2024). Subduction Interface Earthquake Rise-Time Scaling
557 Relations. *Bulletin of the Seismological Society of America*, *114*(1), 278–290.
558 https://doi.org/10.1785/0120230129
559 Cirella, A., Piatanesi, A., Tinti, E., Chini, M., & Cocco, M. (2012). Complexity of the rupture process during
560 the 2009 L'Aquila, Italy, earthquake: Source complexity of the L'Aquila Earthquake. *Geophysical*
561 *Journal International*, *190*(1), 607–621. https://doi.org/10.1111/j.1365-246X.2012.05505.x
562 Diao, H., Ren, Y., Wen, R., Si, H., & Koketsu, K. (2025). Supershear rupture process of the 2025 Myanmar
563 earthquake as derived from joint inversion of near-field and teleseismic waveforms. *Earthquake*
564 *Engineering and Engineering Vibration*, *24*(4), 917–925. https://doi.org/10.1007/s11803-025-2347-
565 z

566 Duputel, Z., Jiang, J., Jolivet, R., Simons, M., Rivera, L., Ampuero, J. -P., Riel, B., Owen, S. E., Moore, A.
567 W., Samsonov, S. V., Ortega Culaciati, F., & Minson, S. E. (2015). The Iquique earthquake sequence
568 of April 2014: Bayesian modeling accounting for prediction uncertainty. *Geophysical Research*
569 *Letters*, *42*(19), 7949–7957. https://doi.org/10.1002/2015GL065402
570 Funning, G. J., Fukahata, Y., Yagi, Y., & Parsons, B. (2014). A method for the joint inversion of geodetic
571 and seismic waveform data using ABIC: Application to the 1997 Manyi, Tibet, earthquake.
572 *Geophysical Journal International*, *196*(3), 1564–1579. https://doi.org/10.1093/gji/ggt406
573 Gabriel, A. -A., Ampuero, J. -P., Dalguer, L. A., & Mai, P. M. (2012). The transition of dynamic rupture
574 styles in elastic media under velocity-weakening friction. *Journal of Geophysical Research: Solid*
575 *Earth*, *117*(B9), 2012JB009468. https://doi.org/10.1029/2012JB009468
576 Gabriel, A. -A., Ampuero, J. -P., Dalguer, L. A., & Mai, P. M. (2013). Source properties of dynamic rupture
577 pulses with off-fault plasticity. *Journal of Geophysical Research: Solid Earth*, *118*(8), 4117–4126.
578 https://doi.org/10.1002/jgrb.50213
579 Goldberg, D. E., Hunsinger, H. E., Koch, P., Haynie, K. L., Melgar, D., & Riquelme, S. (2026). Wavelet
580 Inversion for SliP (WISP): Open-Source Earthquake Slip Modeling Software. *Seismological Research*
581 *Letters*. https://doi.org/10.1785/0220250055
582 Goldberg, D. E., Koch, P., Melgar, D., Riquelme, S., & Yeck, W. L. (2022). Beyond the Teleseism:
583 Introducing Regional Seismic and Geodetic Data into Routine USGS Finite-Fault Modeling.
584 *Seismological Research Letters*, *93*(6), 3308–3323. https://doi.org/10.1785/0220220047
585 Graves, R. W., & Pitarka, A. (2010). Broadband Ground-Motion Simulation Using a Hybrid Approach.
586 *Bulletin of the Seismological Society of America*, *100*(5A), 2095–2123.
587 https://doi.org/10.1785/0120100057
588 Gusev, A. A., & Chebrov, D. (2019). On Scaling of Earthquake Rise-Time Estimates. *Bulletin of the*
589 *Seismological Society of America*, *109*(6), 2741–2745. https://doi.org/10.1785/0120180214

590 Hayes, G. P. (2017). The finite, kinematic rupture properties of great-sized earthquakes since 1990. *Earth*
591 *and Planetary Science Letters*, *468*, 94–100. https://doi.org/10.1016/j.epsl.2017.04.003
592 Heaton, T. H. (1990). Evidence for and implications of self-healing pulses of slip in earthquake rupture.
593 *Physics of the Earth and Planetary Interiors*, *64*(1), 1–20. https://doi.org/10.1016/0031-
594 9201(90)90002-F
595 Hunter, J. D. (2007). Matplotlib: A 2D graphics environment. *Computing in Science & Engineering*, *9*(3),
596 90–95. https://doi.org/10.1109/MCSE.2007.55
597 Ji, C., Wald, D. J., & Hemberger, D. V. (2002). Source Description of the 1999 Hector Mine, California,
598 Earthquake, Part I: Wavelet Domain Inversion Theory and Resolution Analysis. *Bulletin of the*
599 *Seismological Society of America*, *92*(4), Article 4. https://doi.org/10.1785/0120000916
600 Kearse, J., & Kaneko, Y. (2025). *Curved fault slip captured by CCTV video during the 2025 Mw 7.7*
601 *Mandalay earthquake*. Geophysics and Seismology. https://doi.org/10.31223/X5TF0B
602 Kiser, E., & Ishii, M. (2012). The March 11, 2011 Tohoku-oki earthquake and cascading failure of the
603 plate interface. *Geophysical Research Letters*, *39*(7), 2012GL051170.
604 https://doi.org/10.1029/2012GL051170
605 Koch, P., Bravo, F., Riquelme, S., & Crempien, J. G. F. (2019). Near-Real-Time Finite-Fault Inversions for
606 Large Earthquakes in Chile Using Strong-Motion Data. *Seismological Research Letters*.
607 https://doi.org/10.1785/0220180294
608 Koch, P., Goldberg, D. E., Hunsinger, H. E., Melgar, D., Riquelme, S., Yeck, W. L., & Haynie, K. L. (2024).
609 *Wavelet and simulated Annealing SliP inversion (WASP)* [Software]. U.S. Geological Survey.
610 https://doi.org/10.5066/P1EKKUNW
611 Konca, A. O., Kaneko, Y., Lapusta, N., & Avouac, J.-P. (2013). Kinematic Inversion of Physically Plausible
612 Earthquake Source Models Obtained from Dynamic Rupture Simulations. *Bulletin of the*
613 *Seismological Society of America*, *103*(5), 2621–2644. https://doi.org/10.1785/0120120358

614 Kostrov, B. V. (1964). Selfsimilar problems of propagation of shear cracks. *Journal of Applied*
615 *Mathematics and Mechanics*, *28*(5), 1077–1087. https://doi.org/10.1016/0021-8928(64)90010-3
616 Kurahashi, S., & Irikura, K. (2011). Source model for generating strong ground motions during the 2011
617 off the Pacific coast of Tohoku Earthquake. *Earth, Planets and Space*, *63*(7), 571–576.
618 https://doi.org/10.5047/eps.2011.06.044
619 Latour, S., Lebihain, M., Bhat, H. S., Twardzik, C., Bletery, Q., Hudnut, K. W., & Passelègue, F. (2025).
620 Direct estimation of earthquake source properties from a single CCTV camera. *Science*, *390*(6772),
621 463–467. https://doi.org/10.1126/science.adz1705
622 Lay, T., Ammon, C. J., Kanamori, H., Koper, K. D., Sufri, O., & Hutko, A. R. (2010). Teleseismic inversion
623 for rupture process of the 27 February 2010 Chile (M_w 8.8) earthquake. *Geophysical Research*
624 *Letters*, *37*(13), 2010GL043379. https://doi.org/10.1029/2010GL043379
625 Lay, T., Kanamori, H., Ammon, C. J., Koper, K. D., Hutko, A. R., Ye, L., Yue, H., & Rushing, T. M. (2012).
626 Depth-varying rupture properties of subduction zone megathrust faults. *Journal of Geophysical*
627 *Research: Solid Earth*, *117*(B4), 2011JB009133. https://doi.org/10.1029/2011JB009133
628 Mai, P. M., & Beroza, G. C. (2000). Source Scaling Properties from Finite-Fault-Rupture Models. *Bulletin*
629 *of the Seismological Society of America*, *90*(3), 604–615. https://doi.org/10.1785/0119990126
630 Mai, P. M., & Thingbaijam, K. K. S. (2014). SRCMOD: An Online Database of Finite-Fault Rupture Models.
631 *Seismological Research Letters*, *85*(6), 1348–1357. https://doi.org/10.1785/0220140077
632 Meier, M., Heaton, T., & Clinton, J. (2016). Evidence for universal earthquake rupture initiation behavior.
633 *Geophysical Research Letters*, *43*(15), 7991–7996. https://doi.org/10.1002/2016GL070081
634 Melgar, D., & Hayes, G. P. (2017). Systematic Observations of the Slip Pulse Properties of Large
635 Earthquake Ruptures. *Geophysical Research Letters*, *44*(19), 9691–9698.
636 https://doi.org/10.1002/2017GL074916

637 Melgar, D., LeVeque, R. J., Dreger, D. S., & Allen, R. M. (2016). Kinematic rupture scenarios and synthetic
638 displacement data: An example application to the Cascadia subduction zone. *Journal of*
639 *Geophysical Research: Solid Earth*, *121*. https://doi.org/doi:10.1002/2016JB013314
640 Melgar, D., Weldon, R., Wang, Y., Bato, M. G., Aung, L. T., Shi, X., Wiwegwing, W., Khaing, S. N., Min, S.,
641 Thant, M., Speed, C., Zinke, R., Fielding, E., Meltzner, A., & Dawson, T. (2025). Supershear source
642 model of the 2025 M7.8 Myanmar earthquake and paleoseismology of the Sagaing Fault: Regions
643 of significant overlap with past earthquakes. *Seismica*, *4*(2).
644 https://doi.org/10.26443/seismica.v4i2.1771
645 Minson, S. E., Simons, M., Beck, J. L., Ortega, F., Jiang, J., Owen, S. E., Moore, A. W., Inbal, A., & Sladen,
646 A. (2014). Bayesian inversion for finite fault earthquake source models – II: The 2011 great Tohoku-
647 oki, Japan earthquake. *Geophysical Journal International*, *198*(2), 922–940.
648 https://doi.org/10.1093/gji/ggu170
649 Petukhin, A., Galvez, P., Somerville, P., Ampuero, J.-P., Mai, P. M., Pitarka, A., Yoshida, K., & Irikura, K.
650 (2025). Insights into Slip-Rate Time Functions, Rupture Parameter Correlations, and Ground
651 Motions from Validated Multicycle Earthquake Ruptures. Bulletin of the Seismological Society of
652 America, 115(4), 1591–1610. https://doi.org/10.1785/0120240235
653 Schmedes, J., Archuleta, R. J., & Lavallée, D. (2010). Correlation of earthquake source parameters
654 inferred from dynamic rupture simulations. *Journal of Geophysical Research: Solid Earth*, *115*(B3),
655 2009JB006689. https://doi.org/10.1029/2009JB006689
656 Shea, H. N., & Barnhart, W. D. (2022). The Geodetic Centroid (gCent) Catalog: Global Earthquake
657 Monitoring with Satellite Imaging Geodesy. *Bulletin of the Seismological Society of America*, *112*(6),
658 2946–2957. https://doi.org/10.1785/0120220072
659 Solares-Colón, M. M., Goldberg, D. E., Melgar, D., Vanacore, E. A., Sahakian, V. J., Yeck, W. L., Hernández,
660 F., & López-Venegas, A. M. (2025). Slow Rupture, Long Rise Times, and Multi-Fault Geometry: The

2020 M6.4 Southwestern Puerto Rico Mainshock. *Geophysical Research Letters*, *52*(8), e2024GL109740. https://doi.org/10.1029/2024GL109740

Solares-Colón, M. M., & Melgar, D. (2026). Earthquakes Source Scaling at Subfault Scales (Supplementary Data) [Data set]. Zenodo. https://doi.org/10.5281/zenodo.19618638

Somala, S. N., Ampuero, J.-P., & Lapusta, N. (2014). Resolution of Rise Time in Earthquake Slip Inversions: Effect of Station Spacing and Rupture Velocity. *Bulletin of the Seismological Society of America*, *104*(6), 2717–2734. https://doi.org/10.1785/0120130185

Somerville, P., Irikura, K., Graves, R., Sawada, S., Wald, D., Abrahamson, N., Iwasaki, Y., Kagawa, T., Smith, N., & Kowada, A. (1999). Characterizing Crustal Earthquake Slip Models for the Prediction of Strong Ground Motion. *Seismological Research Letters*, *70*(1), 59–80. https://doi.org/10.1785/gssrl.70.1.59

Suhendi, C., Li, B., Vasyura-Bathke, H., Liu, J., Jónsson, S., & Mai, P. M. (2024). Bayesian inversion and quantitative comparison for bilaterally quasi-symmetric rupture processes on a multisegment fault in the 2021 *Mw* 7.4 Maduo earthquake. *Geophysical Journal International*, *240*(1), 673–695. https://doi.org/10.1093/gji/ggae398

Vasyura-Bathke, H., Dettmer, J., Steinberg, A., Heimann, S., Isken, M. P., Zielke, O., Mai, P. M., Sudhaus, H., & Jónsson, S. (2020). The Bayesian Earthquake Analysis Tool. *Seismological Research Letters*, *91*(2A), 1003–1018. https://doi.org/10.1785/0220190075

Vera, F., Carrillo-Ponce, A., Crosetto, S., Kosari, E., Metzger, S., Motagh, M., Liang, Y., Lyu, S., Petersen, G., Saul, J., Sudhaus, H., Symmes-Lopetegui, B., Than, O., Xiao, H., & Tilmann, F. (2025). Supershear Rupture Along the Sagaing Fault Seismic Gap: The 2025 Myanmar Earthquake. *The Seismic Record*, *5*(3), 289–299. https://doi.org/10.1785/0320250025

683 Wang, Y., & Day, S. M. (2017). Seismic source spectral properties of crack-like and pulse-like modes of
684 dynamic rupture. *Journal of Geophysical Research: Solid Earth*, *122*(8), 6657–6684.
685 https://doi.org/10.1002/2017JB014454
686 Wei, S., Wang, X., Li, C., Zeng, H., Ma, Z., Shi, Q., Chen, H., Huang, Y., Lyu, M., Liao, J., Yang, S., Bai, Y.,
687 Maung, P. M., Oo, K., Htwe, Y. M. M., Zhang, J., Dal Zilio, L., Shan, X., & Chen, L. (2025). Supershear
688 rupture sustained through a thick fault zone in the 2025 M_w 7.8 Mandalay earthquake. *Science*,
689 *390*(6772), 468–475. https://doi.org/10.1126/science.adz2101
690 Xu, L., Meng, L., Yunjun, Z., Yang, Y., Wang, Y., Hu, C., Weng, H., Xu, W., Su, E., & Ji, C. (2025). Bimaterial
691 effect and favorable energy ratio enabled supershear rupture in the 2025 Mandalay earthquake.
692 *Science*, *390*(6772), 476–481. https://doi.org/10.1126/science.ady6100
693 Ye, L., Lay, T., & Kanamori, H. (2025). The 28 March 2025 Mw 7.8 Myanmar Earthquake: Preliminary
694 Analysis of an ~480 km Long Intermittent Supershear Rupture. *The Seismic Record*, *5*(3), 260–269.
695 https://doi.org/10.1785/0320250021
696 Ye, L., Lay, T., Kanamori, H., & Rivera, L. (2016). Rupture characteristics of major and great ($M_w \geq 7.0$)
697 megathrust earthquakes from 1990 to 2015: 1. Source parameter scaling relationships. *Journal of*
698 *Geophysical Research: Solid Earth*, *121*(2), 826–844. https://doi.org/10.1002/2015JB012426

Journal of Geophysical Research: Solid Earth

Supporting Information for

Earthquakes Source Scaling at Subfault Scales

M. M. Solares-Colón[1] and D. Melgar[1]

[1]Department of Earth Sciences, University of Oregon, Eugene, Oregon, U.S.A.

Contents of this file

Introduction

This supplement contains auxiliary information on methods and results. Text S1 describes the Bayesian approach used to estimate source scaling laws and Table S1 summarizes the regression results. Figure S1 provides an example of the source parameter estimation using the Bayesian approach. Figure S2 shows comparison of WASP (now WISP) solutions using teleseismic data only inversions versus joint inversions with mixed datasets for four earthquakes from Goldberg et al. (2022) using subfault per parent earthquake. Figure S3 shows mean behavior of earthquake source parameters for each event in the catalog. Figure S4 compares local rise time and rupture duration. Figure S5 and S6 show local behavior of rise time and slip rates by fault type at the subfault scale, respectively. Figure S7 shows resulting slip rates from a rupture simulation of a **M**8.78 in the Cascadia subduction zone with two rise-time assumptions: case (1) includes a prescribed correlation between rise time and slip (Eq. 2; scaling exponent from Melgar & Hayes, 2017), whereas case (2) assumes no dependence of rise time on slip. The full rupture sequence is shown in Video S1.

Text S1. Bayesian Estimation of Source Scaling Laws.

We model the scaling relationship as $\log_{10}(S) = a + b\log_{10}(M_0)$ where S is the source parameter, M_0 is seismic moment, a is the intercept, and b is the scaling exponent. To quantify uncertainty in these parameters, we estimate their posterior distributions using a Markov chain Monte Carlo (MCMC) approach implemented in PyMC4 (Abril-Pla et al., 2023). Sampling is performed with the No-U-Turn Sampler (NUTS) using four chains, 1000 tuning steps, and 2000 posterior samples per chain. Posterior means, covariances, and 95% credible intervals are derived from the sampled distributions. This implementation replaces the original MCMC scheme in Melgar & Hayes (2017) with a more efficient Hamiltonian Monte Carlo method while preserving the underlying statistical model.

Table S1. Source Scaling Regression Results.

Regression Variable (S)	a_{preff}	S_{aa}	b_{preff}	S_{bb}	S_{ab}
Mean Rise Time (s)	-4.560430	0.077532	0.262524	0.000188	-0.003815
Mean Pulse Length (km)	-3.838923	0.067452	0.249160	0.000163	-0.003314
Mean Slip (km)	-6.756323	0.269253	0.343151	0.000651	-0.013232
Source Duration (s)	-5.727985	0.134198	0.353073	0.000324	-0.006593

Note: We model the scaling relationship as $\log_{10}(S) = a + b\log_{10}(M_0)$ and estimate posterior distributions of a and b using a MCMC approach. a_{preff} and b_{preff} are the posterior mean estimates of the regression parameters. S_{aa} and S_{bb} correspond to the variances of a and b, respectively, and S_{ab} is the covariance.

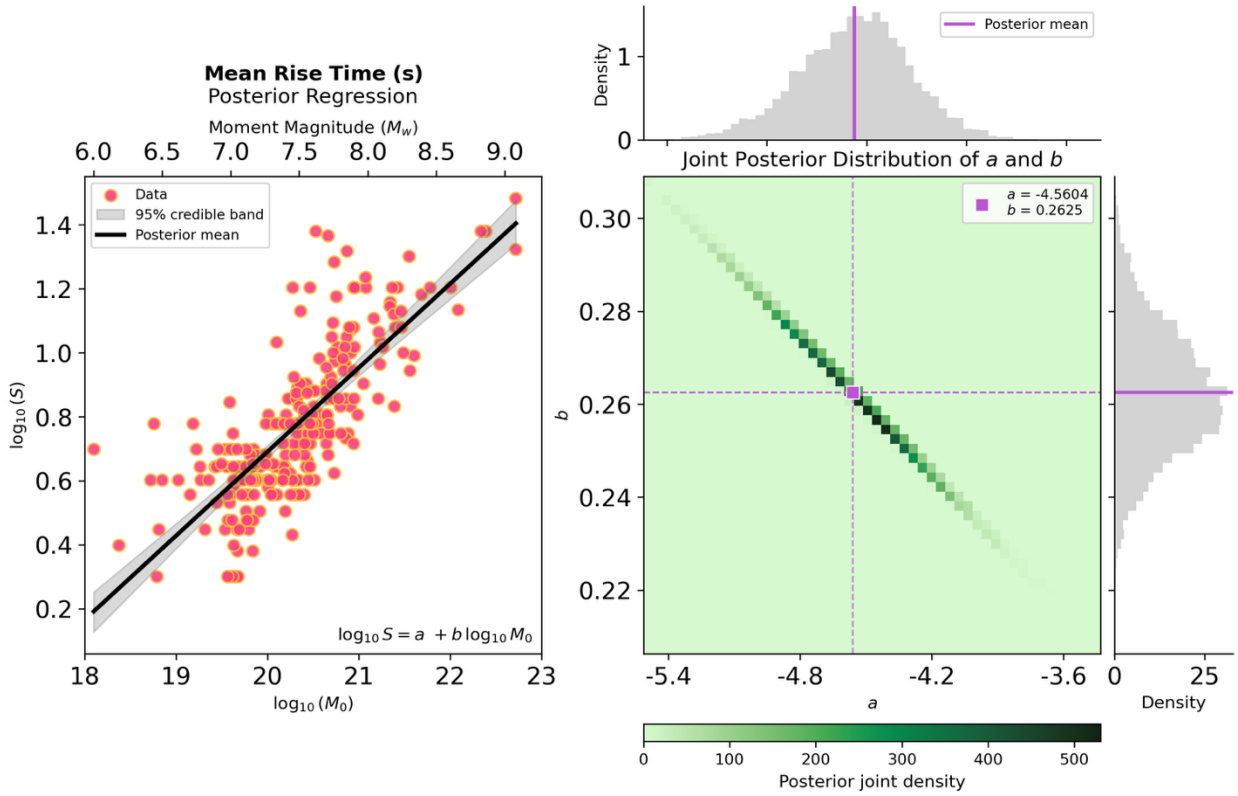

Figure S1. MCMC results for mean rise time as a function of moment. The first panel shows the posterior regression for the source parameter; circles represent mean rise time values for each event in the catalog. The black line denotes the posterior mean regression, and the gray shading indicates the 95% credible band. The second panel shows the joint posterior distribution of a and b, along with the marginal posterior distributions for each parameter; the square and lines mark the posterior mean (a, b), with the dashed lines serving as visual guides to the mean values. The color bar represents the joint posterior density, indicating the relative probability of different combinations of intercept and slope.

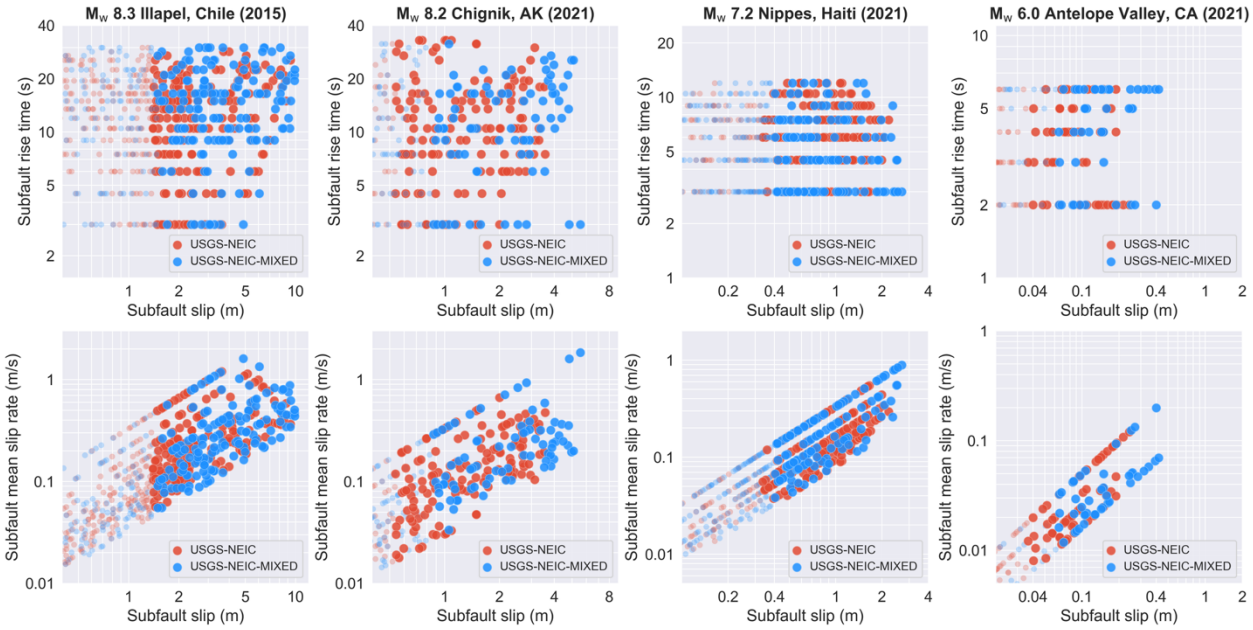

Figure S2. Comparison of WASP rupture models using teleseismic data only versus joint inversions with mixed datasets for four earthquakes from Goldberg et al. (2022): **M**8.3 Illapel (Chile) 2015, **M**8.2 Chignik (Alaska; AK) 2021, **M**7.3 Nippes (Haiti) 2021,and **M**6.0 Antelope Valley (California; CA) 2021. Each column corresponds to one event; the top row shows subfault slip versus rise time, and the bottom row shows subfault slip versus mean slip rate. Red–orange markers denote teleseismic-only NEIC inversion models, while blue markers represent joint inversion models for the same earthquakes. Subfaults with slip ≥ 15% of the event peak slip are emphasized; lower-slip patches are shown smaller and with increased transparency for context.

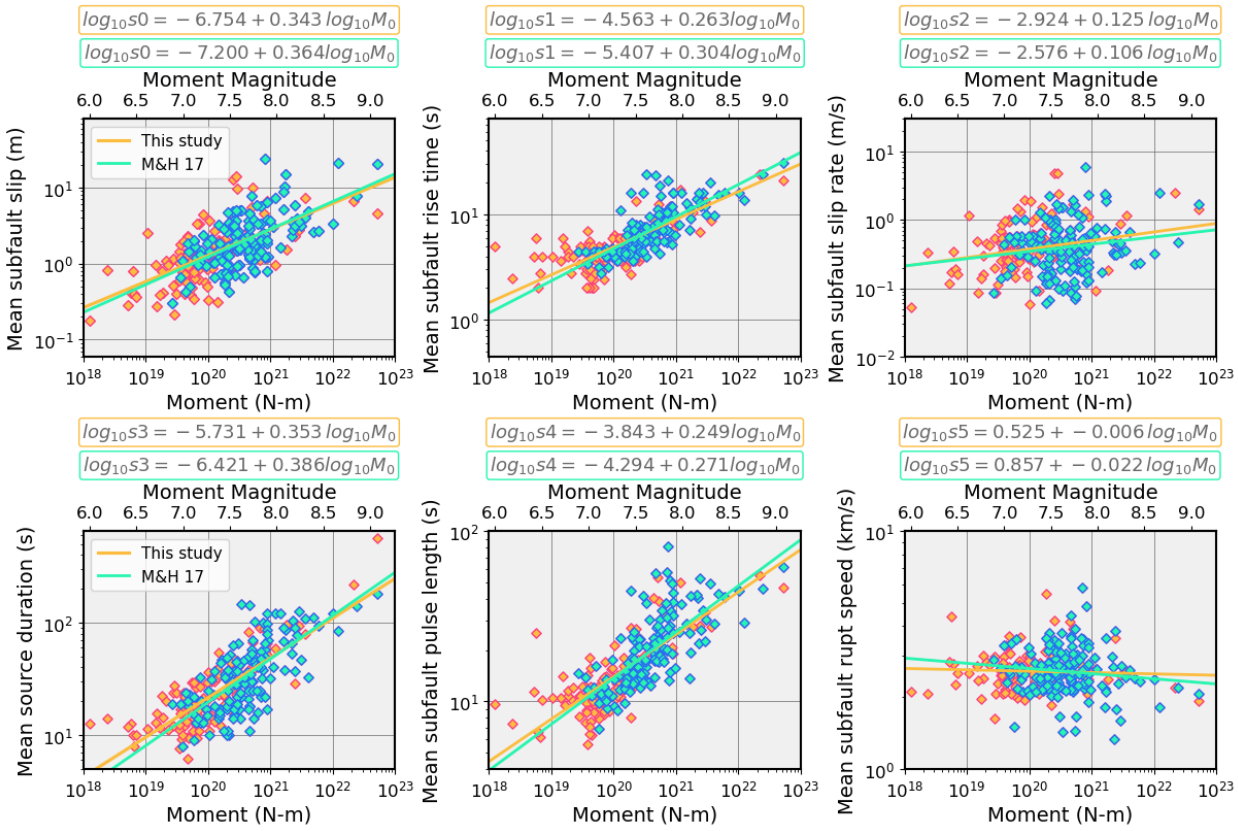

Figure S3. *General behaviors of earthquake source parameters.* Top row: log–log scatter plots of mean subfault slip (left), rise time (middle), and slip rate (right) versus seismic moment for two finite-fault model catalogs. Bottom row: log–log scatter plots of source duration (left), mean subfault pulse length (middle), and mean subfault rupture speed (right) versus seismic moment for two finite-fault model catalogs. Melgar & Hayes (2017) catalog is shown in cool colors (blues, cyan), while newly added events in this study are shown in warm colors (dark pink and yellow) using subfaults with >20% of the maximum slip of each parent earthquake, lines show fitted linear trends through all subfaults. There are a couple discrepancies that exist between the values obtained here for Melgar & Hayes (2017) catalog and the ones reported on the original study that have to do with methodological choices. First, the hypocenter used for this study reflects the one from the finite fault model product and not the event origin product from the USGS event page. Second, a computational error when obtaining the slip rate was discovered, and now the mean slip rate values consider the average across the entire fault per parent earthquake.

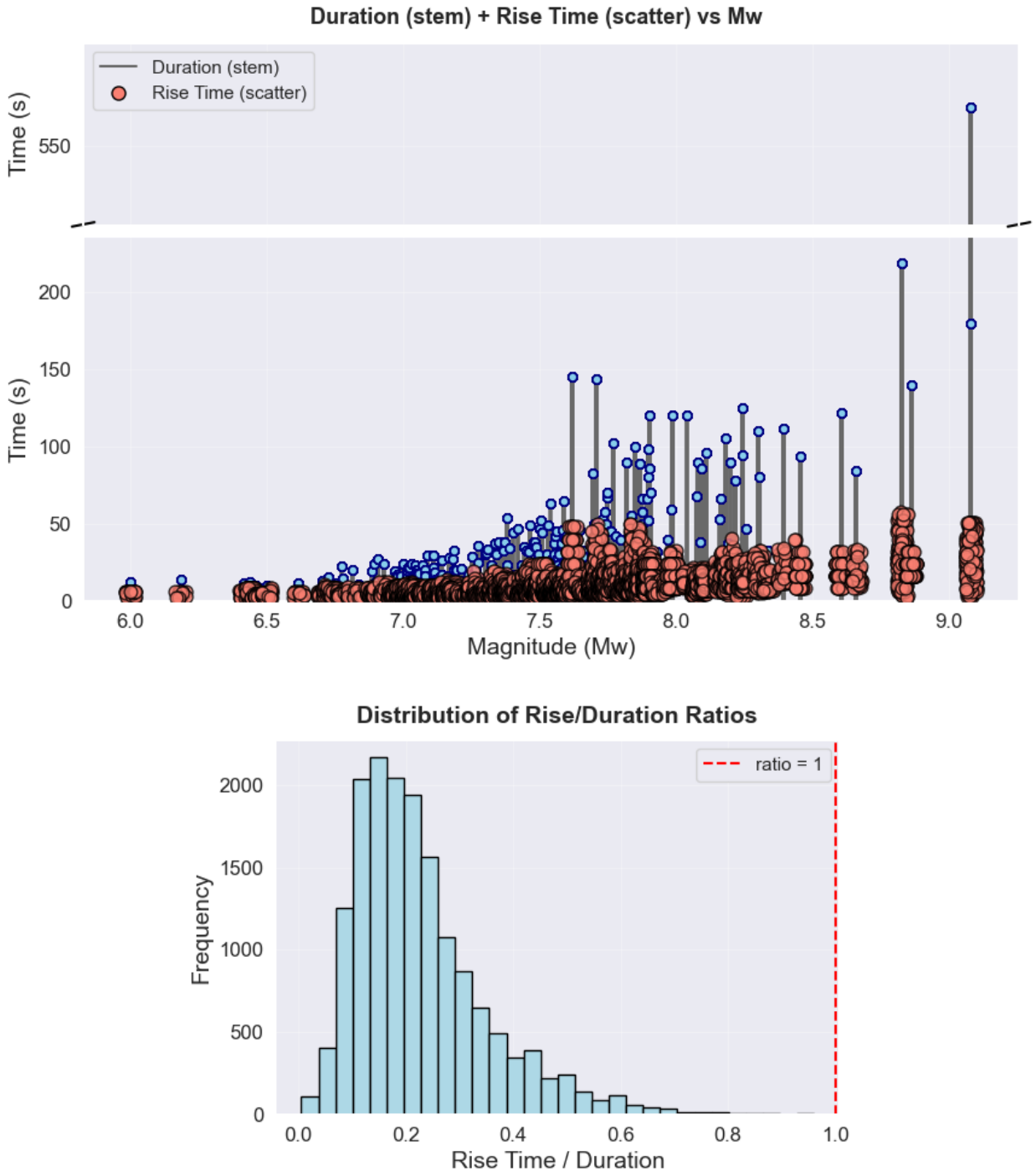

Figure S4. Comparison between rupture duration and local rise time. Top panel shows rupture duration (blue stems) and local rise times (red circles) as a function of moment magnitude (Mw) for all events in the finite-fault model catalog. Both parameters increase with magnitude, though rise times remain systematically shorter than total rupture durations. (Bottom) Histogram of rise-time-to-duration ratios, showing that most subfaults rupture over a fraction (0.1–0.4) of the total event duration (red dashed line marks ratio = 1).

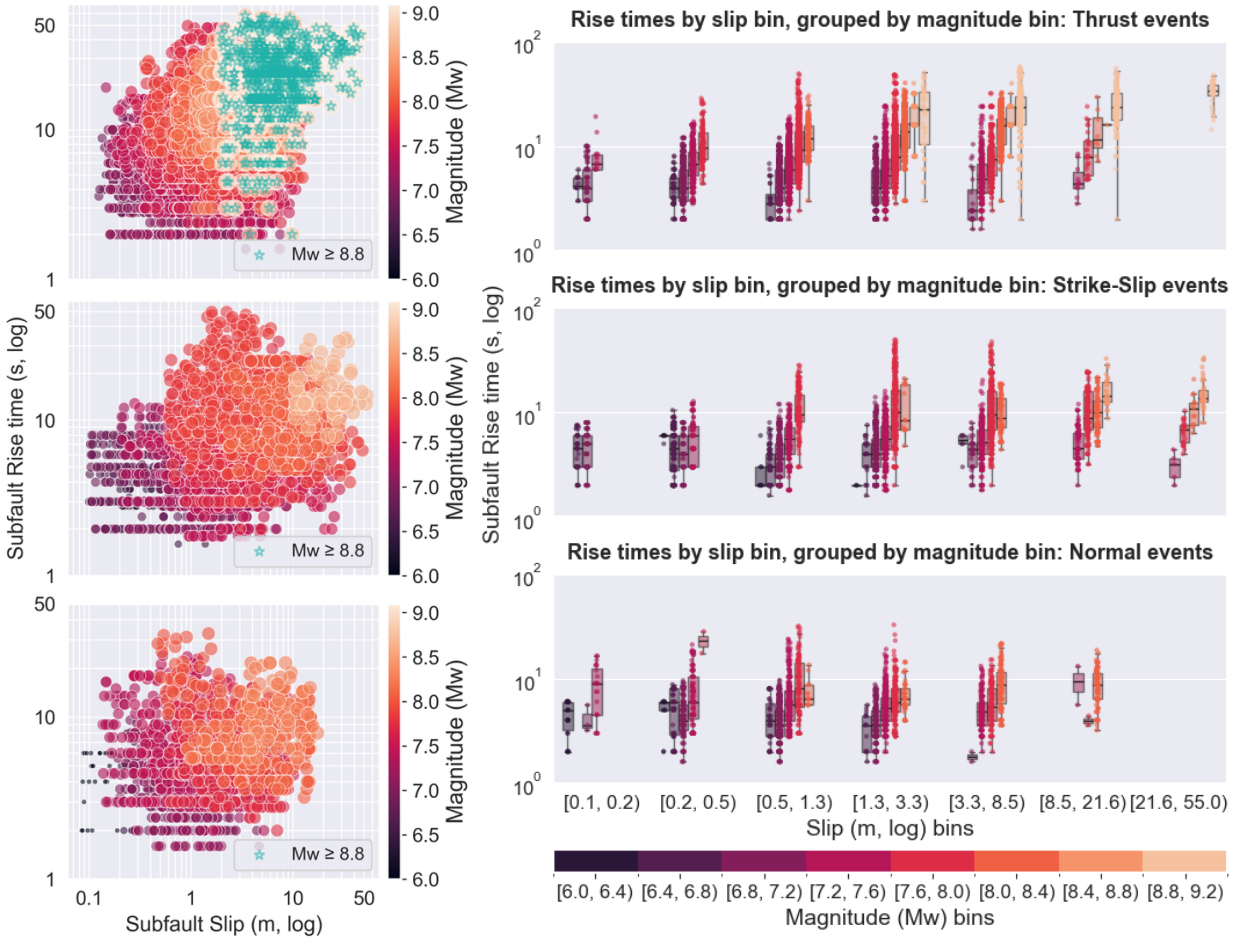

Figure S5. Local behavior of rise time by fault type at the subfault scale. The first panel shows rise time by fault type as functions of slip, with markers colored by magnitude; green stars represent subfaults of the largest events (**M** ≥ 8.8). The second panel presents rise time boxplots by fault type, where subfaults are first binned by slip, and within each bin values are grouped by magnitude—corresponding to the scatter plots in the first panel. From top to bottom, rows show thrust, strike-slip, and normal events.

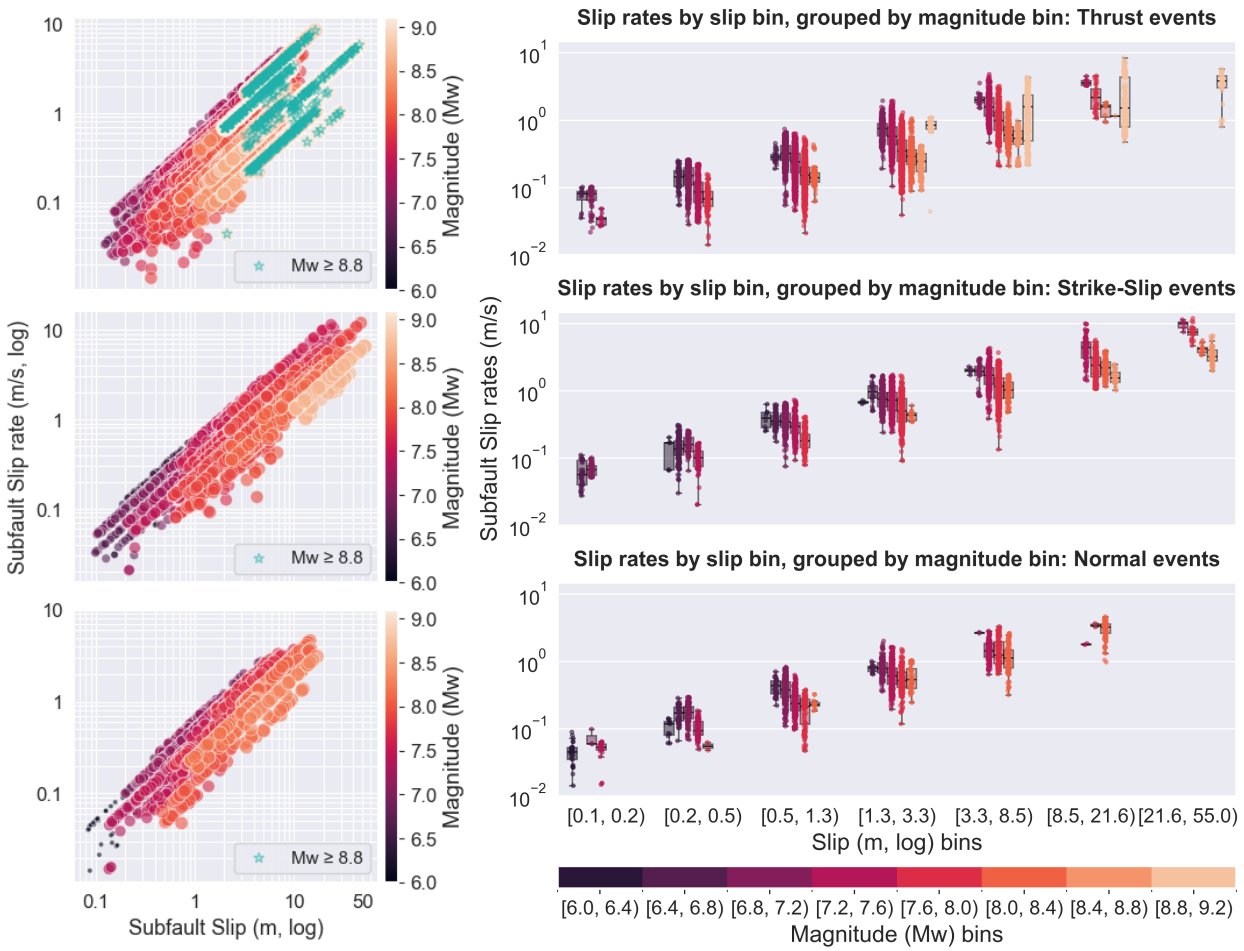

Figure S6. Local behavior of slip rates by fault type at the subfault scale. The first panel shows rise time by fault type as functions of slip, with markers colored by magnitude; green stars represent subfaults of the largest events (**M** ≥ 8.8). The second panel presents slip rates boxplots by fault type, where subfaults are first binned by slip, and within each bin values are grouped by magnitude—corresponding to the scatter plots in the first panel. From top to bottom, rows show thrust, strike-slip, and normal events.

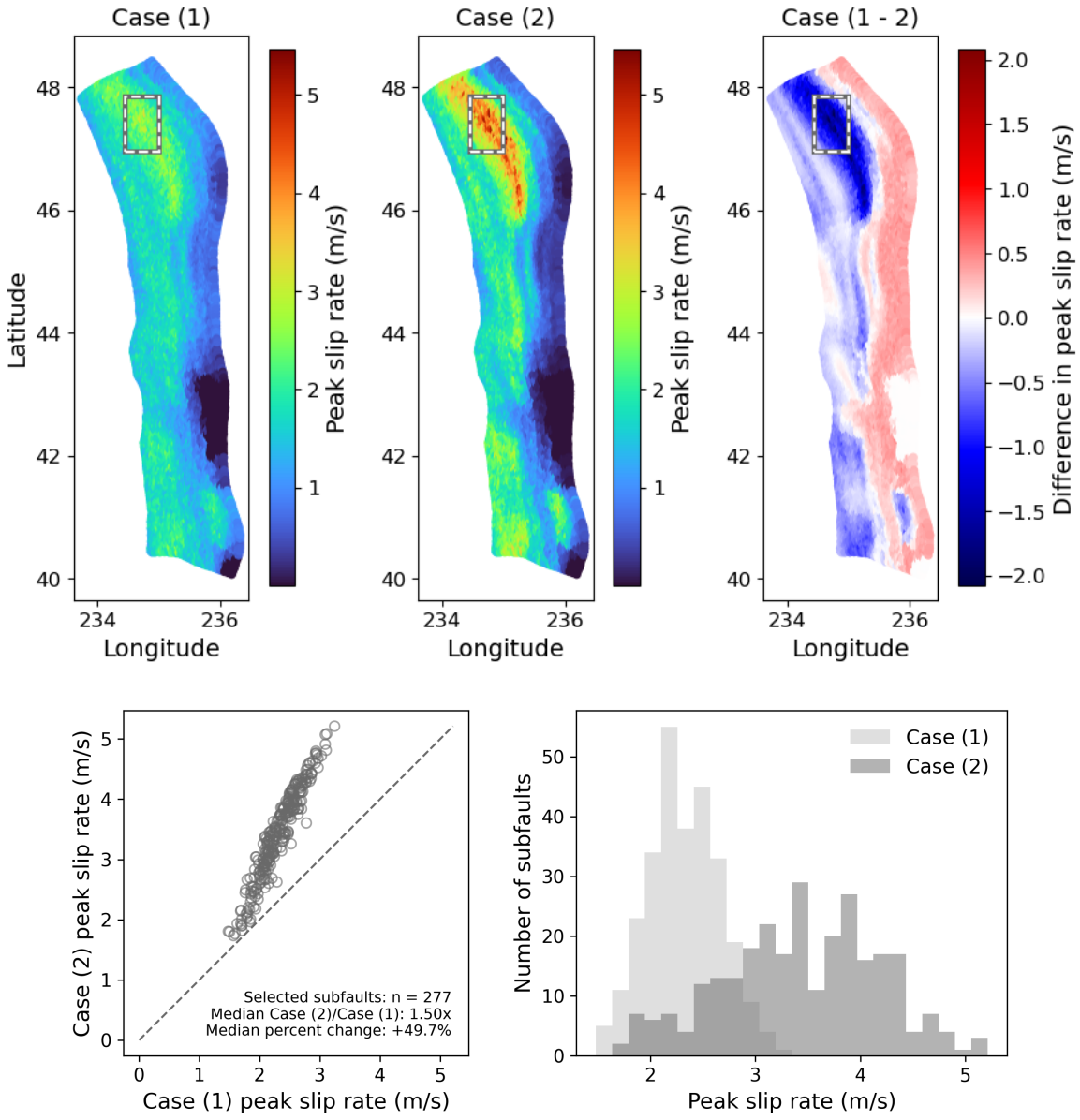

Figure S7. Resulting peak slip rates from a simulated Mw 8.78 rupture in the Cascadia subduction zone. The top row compares two slip–rise-time assumptions. The first column shows Case (1), which includes a prescribed correlation between rise time and slip following Eq. 2, using the scaling exponent from Melgar and Hayes (2017). The second column shows Case (2), which assumes no dependence of rise time on slip. The third column shows the peak slip-rate difference between the two cases, computed as Case (1) minus Case (2); blue indicates areas where Case (2) produces higher peak slip rates, whereas red indicates areas where Case (1) produces higher peak slip rates. The dashed rectangle marks the region selected for subfault-level comparison in the bottom row. The bottom row summarizes peak slip rates for subfaults within this selected region. The left panel shows a one-to-one

comparison between cases, with the dashed line indicating equal values. The right panel shows the corresponding peak slip-rate distributions for the same subfaults. The full rupture sequence is provided in Video S1 of the Supplementary Information.

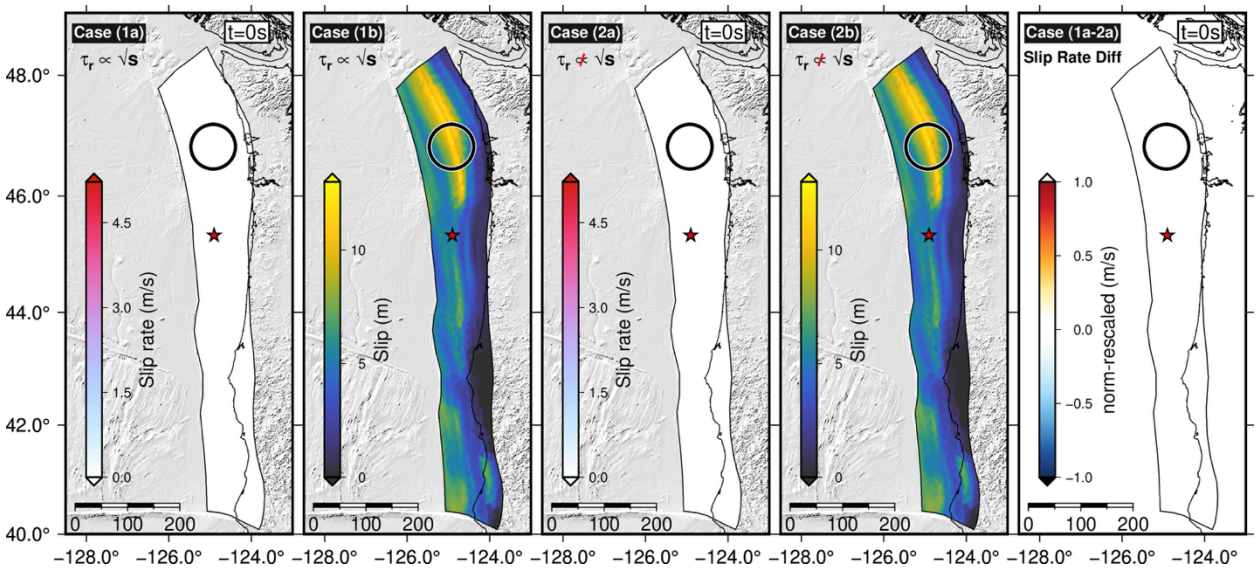

Video S1. Rupture simulation of a **M**8.78 in the Cascadia subduction zone under two rise-time assumptions: case (1) includes a prescribed correlation between rise time and slip (Eq. 2; scaling exponent from Melgar & Hayes, 2017), whereas case (2) assumes no dependence of rise time on slip. Each of the three rows shows a different time step in the rupture evolution, with five panels per row: the first two panels show slip rate and slip for case (1); the next two panels show the same quantities for case (2); and the last panel shows the slip-rate difference between them; black circles are focus points to compare slip pulse width. Blue indicates areas where case (2) produces higher slip rates, and red indicates areas where case (1) produces higher slip rates.